1
2
Wide and Deep Imaging of Neuronal Activities by a Wearable NeuroImager Reveals Premotor Activity in the Whole Motor Cortex
5

Takuma Kobayashi[1]*, Tanvir Islam[1], Masaaki Sato[2,3,4], Masamichi Ohkura[2,3], Junichi Nakai[2,3], Yasunori Hayashi[3,5,6], Hitoshi Okamoto[1]*

8

1. Laboratory for Neural Circuit Dynamics of Decision Making, RIKEN Center for Brain Science, Wako, Saitama 351-0198, Japan
2. Graduate School of Science and Engineering, Saitama University, Saitama, 338-8570, Japan
3. Brain and Body System Science Institute, Saitama University, Saitama, 338-8570, Japan
4. Laboratory for Mental Biology, Brain Science Institute, RIKEN, Wako, Saitama 351-0198, Japan
5. RIKEN Center for Brain Science, Wako, Saitama 351-0198, Japan
6. Department of Pharmacology, Kyoto University Graduate School of Medicine, Kyoto 606-8501, Japan

20

*Corresponding author. Tel.: +81 48 467 9713; Fax.: +81 48 467 9714.
E-mail address: takuma.kobayashi@riken.jp; dr.takuma.kobayashi@gmail.com (T. Kobayashi), hitoshi.okamoto@riken.jp (H. Okamoto)
24
25

Author Contributions:
H.O. and T.K. conceived and designed the research, and wrote the paper. T.K. constructed the imaging system and the experimental apparatus, and performed all experiments. T.I. performed NMF. M.S., M.O., J.N. and Y.H. made the G-CaMP7 transgenic mouse lines.

31

Competing Financial Interests Statement: The authors declare no competing financial interests.
34
35
36

Summary

Wearable technologies for functional whole brain imaging in freely moving animals would advance our understanding of cognitive processing and adaptive behavior. Fluorescence imaging can visualize the activity of individual neurons in real time, but conventional microscopes have limited sample coverage in both the width and depth of view. Here we developed a novel head-mounted laser camera (HLC) with macro and deep-focus lenses that enable fluorescence imaging at cellular resolution for comprehensive imaging in mice expressing a layer- and cell type-specific calcium probe. We visualized orientation selectivity in individual excitatory neurons across the whole visual cortex of one hemisphere, and cell assembly expressing the premotor activity that precedes voluntary movement across the motor cortex of both hemispheres. Including options for multiplex and wireless interfaces, our wearable, wide- and deep-imaging HLC technology could enable simple and economical mapping of neuronal populations underlying cognition and behavior.

1. Introduction

Wearable imaging instruments represent an emerging class of powerful and versatile measurement tools for *in vivo* functional analysis of the brain in freely moving animals[1-4]. Wearable microscopes such as head-mounted 2-photon microscopes, miniature endoscopes, fiber photometers, and other implantable devices have already made significant contributions in neuroscience[5-9]. Many of these instruments also incorporate recent improvements in fluorescent probe technology, such as the genetically encoded Ca^{2+} indicators[10-13], which enable long-period, real-time imaging of neuronal activity at high signal-to-noise ratios in the living animal brain. Despite such advances, wide-field imaging of cortico-cortical inter-regional interactions at high spatiotemporal resolution remains difficult. Most current instruments only allow the capture of images from a single or limited number of focal planes. Also, because ongoing animal movement often breaks the instrument, continuation of the experiment can be difficult if a device is too delicate and expensive to obtain replacements. To address these problems, we developed a novel wearable fluorescence imaging system containing a head-mounted laser camera (HLC) with deep-focus and macro photographic lenses that can comprehensively analyze neuronal activity in the mouse cerebral cortex.

Traditionally, researchers have attempted to improve microscopic optics to obtain wider and deeper fields of view under the restricting design conditions of a defined focal plane and optical aberration correction. Here, we tried to achieve the same goal, but with an alternative approach using a deep-focus optical system that can integrate images of objects at different depths and perspectives into a single-plane image. This apparatus adopts an optical system similar to the one used in inexpensive compact cameras and smart cellular phones, thereby allowing us to obtain images similar to the z-stack images of multiple focal planes produced by two-photon laser microscopy. Many types of camera modules are commercially available, thus we could manufacture a compact HLC imaging system on a purpose-built or mass-production commercial scale, and within a reasonable budget.

In this study, we used a hand-made HLC for *in vitro* and *in vivo* fluorescence Ca^{2+} imaging to assess whether physiological neuronal activity could be visualized over a wide view in the deep cortical layers of a freely moving mouse. We also show that we can resolve the information of activities of individual cells

93 by application of proper image processing algorithm. First, we imaged individual
94 neurons with orientation selectivity in the visual cortex to analyze cellular
95 physiology, and second, we applied the HLC to identify the cellular assembly
96 used for premotor activity during the planning phase before the initiation of
97 voluntary movement in the motor cortex of both hemispheres.
98
99
100
101 **2. Results**
102
103 2.1 Development of a wearable instrument for fluorescence imaging of neural
104 activity in the cerebral cortex.
105
106 Figure 1 demonstrates our wearable fluorescence imaging system
107 developed to visualize neural activity in the cerebral cortex of freely moving mice
108 (left panel in Fig. 1a, b, Methods section; surgical method is explained in
109 Supplementary Fig. 1a). The wearable apparatus consists of a separable
110 camera and a spacer with a cranial window at its base. Imaging of the cortex is
111 performed by the camera component through the cranial window. The object
112 plate of the cranial window makes direct contact with the surface of the cortex
113 (Fig. 1b). Repeated imaging of a specific brain area can be easily carried out
114 while housing the mouse for a long period (Supplementary Fig. 1b). By
115 equipping a suitable excitation light source and an absorption filter, the HLC can
116 perform imaging for green or red fluorescence (right panels in Fig. 1a). The HLC
117 is compact and lightweight, and therefore does not impede an animal's normal
118 behavior (Fig. 1c, Supplementary Movie 1). We confirmed that the imaging of
119 neuronal activities by the HLC attached to the head of freely moving mice
120 causes no significant increase of stress, and does not affect the locomotor
121 activity and the behavioral pattern (Supplementary Fig. 2).
122 Additionally, multiple cameras can be attached to the heads of small mice
123 such as the C57BL/6 line (Fig. 1c, Supplementary Fig. 1c-e) to enable the
124 simultaneous imaging of multiple loci, which previously has proved difficult.
125 Importantly, since the wearable HLC is robustly fixed to the mouse skull, normal
126 body movements do not perturb the wide-view fluorescence imaging (Fig. 1d,
127 Supplementary Movie 2). The number of blinking spots representing
128 presumptive cellular elements in the field of view in Fig. 1d was estimated at

129   approximately 10,000 (Supplementary Fig. 3, Supplementary Movie 3).

130   We used a laser diode (LD) in the HLC as an excitation light source. Thus,

131   to prevent possible temperature increases in the diode due to continuous lighting

132   during long-term imaging, we tested an LD driver with an attached pulse

133   generator to toggle the LD on and off (Supplementary Fig. 4a) and heat sinks of

134   different sizes. This modified design seemed to effectively suppress temperature

135   changes in the LD that could adversely affect the neuronal imaging

136   (Supplementary Fig. 4b-f). Furthermore, pulse driving strengthens the laser light,

137   and such an integrated light source makes the system more adaptable to

138   wireless control than one dependent on an external light source via optical fiber

139   (Supplementary Fig. 5). Therefore, the HLC imaging system is suitable for use

140   on constantly moving animals by using either wired or wireless transmission

141   because the number of output channels is small enough to allow a USB

142   connection and low electric power consumption with a CMOS image sensor.

143   Before moving to *in vivo* imaging, the *in vitro* optical specifications of the

144   HLC were investigated (Fig. 2a-f, Methods section). A checkerboard chart (Fig.

145   2a, b) or a line chart (Fig. 2c-f) was captured by the HLC, and each optical

146   parameter was calculated based on the actual measurement values. As a result,

147   a maximum spatial resolution 4.17 µm/pixel was obtained if the blurring of edges

148   in the images were ignored (Fig. 2a). The optical distortion was 2.78% at

149   maximum (television distortion = 3.91%), and the depth of field exceeded 19.5

150   mm (see Methods section for details of the calculations).

151   Next, the optical processing conditions for homogenizing the flat irradiation

152   shape of a coherent laser beam emitted by the LD were examined using a

153   light-shaping diffuser (LSD) (Fig. 2g, h, Supplementary Fig. 4g, h). Based on

154   actual measurements using various types of LSD (Fig. 2h) and comparison with

155   the theoretical value with simulation (Supplementary Fig. 4g, h), a 60 x 10

156   degree LSD was found to be the most preferable. Accordingly, we expected that

157   the HLC equipped with a deep-focus optical system could capture images from

158   wide brain areas and various depths at quasi-cellular resolution.

159   To verify the imaging ability of the HLC, *in vitro* and *in vivo*

160   fluorescence-imaging tests were performed. First, images of the fluorescent

161   beads implanted into the cerebral cortex of the mouse were compared between

162   the HLC and a conventional stereomicroscope (Fig. 3a-c). The HLC, but not the

163   conventional stereomicroscope could detect beads of similar size to cells in the

164   deep cortex even at 800 µm in depth (Fig. 3d, e). Additionally, the deep-position

165 HLC images showed less blurring of the bead shapes than those taken by
166 stereomicroscope (Fig. 3f). The findings indicate that the HLC can acquire
167 fluorescence signals deep in the cerebral cortex at high precision compared to a
168 conventional wide-field fluorescence microscope. Second, the Ca^{2+} imaging was
169 performed with 3D cultured cells made by embedding transfected Hela cells in
170 an extracellular matrix gel as a mock brain tissue (Fig. 4a). The change ratios
171 ($\Delta F/F$) of the fluorescence intensity (FI) of individual cells at various depths
172 increased with histamine administration, whereas they were decreased by EGTA
173 administration (Fig. 4b, Supplementary Fig. 6a, Supplementary Movie 4). The
174 results indicate that the Ca^{2+} imaging of individual cells could be performed in a
175 3D cell culture using the HLC.

176 The spacer part of the device with the cranial window is also useful to
177 observe the cortex under a conventional or 2-photon microscope system
178 (Supplementary Fig. 7, Supplementary Movie 5); however, a major advantage of
179 the HLC in this regard is that a large amount of information can be obtained from
180 a single image in real time compared to scanning multiple focal planes as
181 needed for the same results by confocal or 2-photon laser microscopy systems.
182 Furthermore, by using transgenic animals expressing the Ca^{2+} indicator
183 fluorescent proteins in layer- or cell type-specific manners, we also obtained
184 images from defined subpopulations of neurons in the brain regardless of their
185 distribution areas. As two examples in the present study, CaMK2a-G-CaMP7
186 mice expressing G-CaMP specifically in excitatory neurons (Fig. 5, 6,
187 Supplementary Fig. 7-9) and Thy1-G-CaMP7 mice expressing G-CaMP
188 predominantly in layer 5/6 pyramidal neurons were imaged (Fig. 4c, d,
189 Supplementary Fig. 6c).

190 For Ca^{2+} imaging of the Thy1-G-CaMP7 mouse by the HLC, we applied an
191 electrical tetanus stimulation to the somatosensory area, and observed an
192 increased FI around the electrode in the transgenic mouse, whereas no such
193 evoked signals were detected in a control wild-type mouse (Fig. 4c, d,
194 Supplementary Fig. 6c, Supplementary Movie 6). In Supplementary Movie 6, the
195 HLC was placed on the surface of the cortex without fixing it to the cranial bone.
196 Therefore, the image shows slight vibrations due to the muscle movement
197 induced indirectly by stimulation of the somatosensory area, even under
198 anesthesia. The imaging result indicates that HLC can visualize the evoked
199 activity of cortical neurons located as deep as layer 5/6.
200

201 2.2 The HLC can detect physiological neuronal activity at cellular resolution in
202 the cerebral cortex including the visual area of one hemisphere in freely moving
203 mice.
204

205   To demonstrate the validity of the HLC, physiological responses of individual
206 neurons during visual perceptual information processing were observed by Ca^{2+}
207 imaging in freely moving CaMK2a-G-CaMP7 mice (Fig. 5-7).
208   By twisting the lens barrel of the camera part of the HLC, the HLC can
209 obtain either a narrow or wide field of view arbitrarily (Fig. 2a, b, Methods
210 section). A short spacer was used to compensate for the reduction in the working
211 distance by optical zooming (Fig. 5a-c). Under the freely moving condition, Ca^{2+}
212 imaging was performed on the visual cortex of the CaMK2a-G-CaMP7 mouse
213 (Fig. 5d, e, Supplementary Movie 7). As a result, the neuronal activity of the
214 visual cortex can be visualized when the mouse was viewing the surrounding
215 scenery, and the vibration derived from mouse's behavior was not observed and
216 the view field did not drift because of the firm attachment of the HLC to the head.
217 It can be noted that the detection of cells with partial overlap in XY plane but
218 separated in Z axis can raise the possibility of simultaneous recording of cells
219 from various layers of the cortex. To address this problem, we deconvoluted the
220 signals of overlapping cells individually by using a NMF (Non-negative Matrix
221 Factorization) algorithm[14] (Fig. 6, Methods section). As a result, 685 cells and
222 their activities were detected in the magnified 600 x 800 μm image (Fig. 6c, d).
223 The HLC captures signals from cells at various depths, superimposed in one
224 plane. Though it is not possible to exactly determine the depth of the cells from
225 the surface with the current HLC, we can roughly assume that cells with higher
226 baseline activities may be located on shallower depth from the surface and
227 reconstruct the putative distribution of cells in 3D (Fig. 6e, f).
228   Next, to examine the differences in physiological responses to different
229 stimuli, a 0.1-second (sec) single flashlight stimulation or 10 repeats of a 0.5-sec
230 flashlight stimulus (light on, 25 ms; light off, 25 ms; 10 times), was applied to the
231 mouse by using an LED positioned in front of the left eye (Methods section).
232 Transient increases (av. 0.50 sec, SD ± 0.14) in FI were observed at 12
233 fluorescence spots in the primary visual cortex (V1) when a flash stimulation was
234 applied (Fig. 7b), whereas gradual increases in the FI of 7 spots were observed
235 over a longer period (av. 1.09 sec., SD = ± 0.41) during and after repeated flash
236 stimuli (Fig. 7c). The ΔF/F at places other than the visual area, considered to

237 represent basal brain activity irrelevant to visual information processing, showed
238 a fluctuation within 3% maximal FI (black line in the graph). No significant
239 increases of the ∆F/F at these places (black line) during the light stimulus mean
240 that no external light was incident on the imaging area and supports the
241 correctness of the experimental results. Evidently, the transient, significant
242 increases of fluorescence in the visual cortex were caused by neuronal activity,
243 and such increases were strong and long depending on the stimulation time.
244 These results demonstrate that the HLC can differentiate the neuronal
245 responses to different stimuli.

246 The complex cells in the primary visual cortex in cats show specific
247 orientation selectivity in response to the specific directions of scanning light
248 stimuli[15]. In rodents, the orientation selectivity is represented mainly in layer 2/3
249 neurons, although minor responses are also observed in the geniculate afferent
250 fibers[16,17]. The neurons with orientation selectivity are also randomly distributed
251 in the visual cortex of rodents, thus we examined whether the HLC could detect
252 such neuronal activity within the visual cortex of mice.

253 An 8-direction drifting grating was presented to the mice, and Ca^{2+} imaging
254 was performed (Fig. 7a, Methods section). A transient, strong increase in FI was
255 detected at the specific light spots in V1 only when a specifically orientated
256 grating was presented (Fig. 7d). The left column graphs indicate the examples of
257 the 15 light spots that responded robustly to 0 and 180-degree stripes (asterisks),
258 and did not respond at all to 90 and 270 degrees. In contrast the right column
259 graphs indicate the examples of the 12 light spots that responded robustly to 90-
260 and 270-degree stripes (asterisks), while none of them responded to 0 and 180
261 degrees. We further analyzed the orientation specificity of all ROIs of the
262 observed area (Fig. 7e-g, see Methods for details). The responding light spots
263 could therefore represent neurons with specific orientation selectivity. Thus, the
264 HLC enables a broad-volume analysis of the physiological activity of single
265 neurons in the cerebral cortex.

266

267 2.3 Functional neuronal imaging of the whole motor cortical area reveals specific
268 patterns of premotor activity representing discrete neuronal assemblies.

269

270 We next explored the advantages of the wearable instrument for the
271 analysis of brain activity in freely behaving subjects, including movement. For
272 this purpose, the entire motor cortex area of a mouse was exposed on the

273 surface of the brain, such that the HLC could visualize the entire area in both

274 hemispheres simultaneously. Ca^{2+} imaging of CaMK2a-G-CaMP mice was

275 performed using the HLC in the frontal cortical area including the motor cortex of

276 freely moving animals (Supplementary Fig. 8). Different patterns of neuronal

277 activity were elicited depending on different external stimulations of the acoustic

278 and somatosensory modalities. Among those event-related responses,

279 synchronized and slow wavelike activities were observed across broad areas

280 while the mouse was standing still after the stimulation (Supplementary Movie

281 8).

282 The pre-motor readiness potential (RP) originally reported as a

283 bereitschaftspotential, is a neuronal premotor activity elicited in the motor

284 cortical area before the initiation of voluntary muscle movement[18]. The RP

285 thought to occur in the higher motor cortex earlier than nerve activity to move the

286 muscle is presumed to be the reflection of the animal's intention to move the

287 body[19,20]. The premotor activity for an unintended action is categorized as a

288 Type-II RP (no preplanning) while the larger premotor activity for an intended

289 action is distinguished as the Type-I RP (preplanned act); however, it is difficult

290 to analyze premotor activity induced by the random behavior of animals, and the

291 observation of a part of the motor cortex alone cannot reveal the entirety of this

292 premotor activity. Therefore, in the present study, we attempted to measure

293 neuronal activity in the whole motor cortical area of the mouse during voluntary

294 movement to verify that a specific cell assembly expressing the readiness

295 potential might exist.

296 We developed what we term "restriction motion experiment" to easily detect

297 the activity associated with a specific movement (Fig. 8, Methods section). In this

298 study, a mouse with the HLC on its head was restrained in a plastic tube with its

299 four legs attached to splints set up for monitoring leg movements (Fig. 8a, b).

300 Brain activity preceding the actual execution of exercise, i.e., the readiness

301 potential, is proposed to occur in the motor cortical area[18], thus we sought to

302 confirm this observation using the HLC on our mouse subjects. Using the

303 movement of a lever as an index, the neuronal activities in bilateral motor

304 cortices were extracted immediately before and after the onset of a specific

305 movement (Fig. 8c, d). First, the locations of neurons activated before and/or

306 after the initiation of motion in the left or right hindleg were either established

307 from raw imaging data by visual judgment of the experimenter (Supplementary

308 Movie 8) or were extracted with a cross-correlation method (Supplementary Fig.

309 9a). As a result, activity in the M2 area on the contralateral side was higher than

310 that on the ipsilateral side (Supplementary Fig. 9a). Therefore, the right and left

311 hindleg movement accompanied the premotor neuronal activity mainly on the

312 contralateral side of the cortical area, which roughly matches the hindleg

313 position in the secondary motor cortex as estimated previously[21]. However, both

314 these detection methods have intrinsic problems, as visual judgment can easily

315 miss important signals, and screening by cross-correlation can also miss the

316 responses of neurons that do not appear in every trial, but may still be

317 physiologically important. Thus, a more comprehensive quantitative analysis

318 was sought by merging the image data of multiple events (11 left leg kicks, 10

319 right leg kicks). The maximum FI value during the period (3 sec) before or after

320 the kick was identified for each pixel, and then this value for each pixel was

321 subtracted by the maximum FI value of the same pixel during three 6-sec

322 periods with no leg movement. The subtracted maximum FI value for each pixel

323 was mapped in the right column images of Fig. 8e where the timing of the

324 emergence of each maximum value was color-coded either in green or red

325 depending on whether it appeared before or after the initiation of leg movement,

326 respectively. We further took into account the frequency of these peaks

327 appearing in all kick events, and Fig. 8f shows the time windows before or after

328 the initiation of leg movement during which each peak appeared (see

329 Supplementary Fig. 9b, c for the detailed process). Different levels of color

330 intensity represent the frequency of appearance, and the different colors

331 represent the timing of the maximum peaks. These results also support the

332 conclusion that leg motion is preceded by premotor activity mainly in the

333 contralateral M2 area as a starting point, and as shown here, the activity started

334 within a period of between -2 sec and -1 sec. This timing supports results using

335 the other methods described above, although the distribution does not strictly

336 follow the conventional M1/M2 division, with the activity propagating from the

337 anterior to the posterior poles and from contralateral to bilateral areas broadly.

338 Further qualitative analysis also supported these results (Supplementary Fig.

339 9d-g), with a cell grouping method based on raw imaging data across the entire

340 motor cortex finding that the cell assembly presenting the pre-motor activities is

341 the main contributor of the lateralized activities both before and after a specific

342 movement (middle graphs of Supplementary Fig. 9d, e). This result suggests

343 that the lateralized activity of the premotor active cell assembly ensures the later

344 lateralized motion. In conclusion, these results indicate that the HLC can

345 visualize specific cell assemblies representing premotor activity in the whole
346 motor cortex (Fig. 8g).
347
348
349

350 **3. Discussion**
351

352 In this study, we describe a wearable imaging system with wide-field,
353 deep-focus optical capabilities that will enable comprehensive physiological
354 analyses of the broad and deep area making up the cerebral cortex. By
355 application of proper image processing algorithm such as NMF, we can also
356 resolve the information of activities of individual cells. In particular, long and
357 continuous (in one day) or longitudinal (over multiple days) observation of the
358 brain in the same individual under free-moving conditions can be performed
359 easily with the HLC. In fact, we observed the light response of the neurons in the
360 visual cortex over multiple days (day1 and 18, or day 11 and 20 after operation).
361 These advantages make the HLC an easy-to-use tool for initial survey analyses
362 prior to using more sophisticated systems for higher resolution studies. To
363 enable better detectability and spatiotemporal resolution, we will need to further
364 improve the optical system and image sensor. In addition, to compensate for the
365 lack of depth information available with HLC imaging, transgenic lines
366 expressing a fluorescent Ca^{2+} indicator could be used to image specific cortical
367 layers or cell types.

368 Various applications for imaging in the present study revealed the
369 visualization of orientation selectivity encoded in individual excitatory neurons
370 within the whole visual cortex of one hemisphere, and also revealed specific cell
371 assemblies representing activation of the entire bilateral motor cortex during
372 volitional behavior output. The firm attachment of the HLC imaging system to the
373 head of a freely moving mouse enables the stable visualization of the neuronal
374 activities in the same field of view at high reproducibility over many days, and the
375 lightweight property of entire imaging system allows the mouse to move freely
376 with relatively a small amount of stress, also permits the simultaneous use of
377 multiple HLCs (Supplementary Fig. 2, Supplementary Movie 10).

378 Various volumetric imaging technologies have been developed recently. For
379 example, in multi-photon microscope technology capable of deep observation, a
380 2P-RAM (2-photon random access mesoscope)[22] provides a wide field of view

381 with high spatial resolution. However, it is impossible to eliminate the time lag for
382 scanning multiple areas in the large field. A wearable endoscope equipped with
383 a light-field optics[23] provides 3D imaging with no time lag but with sacrifice of
384 spatial resolution, but it requires a large amount of calculation for the
385 reconstruction of 3D image. On the other hand, a method of 3D imaging by
386 combining a light-field or HiLo (highly inclined and laminated optical sheet)
387 microscopy with a stage system that keeps up with fast motion of an animal was
388 developed[24,25]. Under the necessity to carry out high-speed tracking at high
389 precision in a fixed direction and the limitation in the size of observation field of
390 view and depth, these system have been applied for the whole-brain Ca^{2+}
391 imaging of the freely moving animals with relatively small bodies such as
392 zebrafish larvae. Some of the above methods require expensive and large-scale
393 equipment.

394   In contrast, among the currently available various wearable optical imaging
395 tools, the HLC is positioned as a unique wide-field, volumetric, and low-invasive
396 imaging device for fluorescence imaging. The HLC in this paper provides a wide
397 field of view and improved detection capability of deep signals. There is no time
398 lag in imaging by the image sensor unlike the galvano scanning system. The
399 laser of the excitation light source provides higher S/N with higher light density
400 than the LED. The spacer apparatus with cranial window can be easily attached
401 to the head with simple surgical operation and enables longitudinal observation
402 over multiple days. Simple mechanisms of the HLC are suitable for commercial
403 production.

404   Fluorescence change was maintained to be observable as long as 57 days
405 after operation (Supplementary Fig. 7e, f). Judging from the observation by
406 stereo microscopy in Supplementary Fig. 1b, meanwhile, the clarity of the cranial
407 window was kept unchanged for 100 days in the same individual. Therefore, we
408 assume that longitudinal Ca^{2+} imaging is possible for at least 3 months. Because
409 we stopped imaging and monitoring within 3 months, it might still be possible to
410 continue observation beyond this period.

411   Although only a few animal experiments were conducted to showcase the
412 utility of the microscope in this paper, in the near future, longitudinal imaging
413 using the wearable HLC tracking the same neurons at the same site under
414 free-movement conditions will help to reveal neuronal activity that is specific to
415 various behavioral tasks. Additionally, the simultaneous use of multiple HLCs will
416 facilitate investigation of cognition and behavior through neuronal activity

417   imaging of the global sensorimotor system in animals, especially by a
418   combination of electrophysiology and optogenetical applications.
419
420
421

422 **Acknowledgements**

423

448
449
450
451

References

1. Schulz, D. et al. Simultaneous assessment of rodent behavior and neurochemistry using a miniature positron emission tomograph. *Nat Methods* **8,** 347-352 (2011).

2. Tang, J. et al. Noninvasive high-speed photoacoustic tomography of cerebral hemodynamics in awake-moving rats. *J Cereb Blood Flow Metab* **35,** 1224-1232 (2015).

3. Miao, P., Lu, H., Liu, Q., Li, Y., Tong, S. Laser speckle contrast imaging of cerebral blood flow in freely moving animals. *J Biomed Opt* **16,** 090502 (2011).

4. Urban, A. et al. Real-time imaging of brain activity in freely moving rats using functional ultrasound. *Nat Methods* **12,** 873-878 (2015).

5. Helmchen, F., Fee, M.S., Tank, D.W. & Denk, W. A miniature head-mounted two-photon microscope: high-resolution brain imaging in freely moving animals. *Neuron* **31,** 903-912 (2001).

6. Zong, W. et al. Fast high-resolution miniature two-photon microscopy for brain imaging in freely behaving mice. *Nat Methods* **14,** 713-722 (2017).

7. Ghosh, K.K. et al. Miniaturized integration of a fluorescence microscope. *Nat Methods* **8,** 871-882 (2011).

8. Hayashi, Y., Tagawa, Y., Yawata, S., Nakanishi, S & Funabiki, K. Spatio-temporal control of neural activity in vivo using fluorescence microendoscopy. *Eur J Neurosci* **36,** 2722-2732 (2012).

9. Kobayashi, T. et al. Optical communication with brain cells by means of an implanted duplex micro-device with optogenetics and Ca^{2+} fluoroimaging. *Sci Rep* **6,** 21247 (2016).

10. Nakai, J., Ohkura, M. & Imoto, K. A high signal-to-noise Ca^{2+} probe composed of a single green fluorescent protein. *Nat Biotechnol* **19,** 137-141 (2001).

11. Zhao, Y. et al. An expanded palette of genetically encoded Ca^{2+} indicators. *Science* **333,** 1888-1891 (2011).

12. Ohkura, M. et al. Genetically encoded green fluorescent Ca^{2+} indicators with improved detectability for neuronal Ca^{2+} signals. *PLoS One* **7,** e51286 (2012).

13. Chen, T.W. et al. Ultrasensitive fluorescent proteins for imaging neuronal activity. *Nature* **499,** 295-300 (2013).

488   14. Maruyama, R. et al. Detecting cells using non-negative matrix factorization
489   on calcium imaging data. *Neural Networks* **55**, 11-19 (2014).

490   15. Hubel, D.H. & Wiesel, T.N. Receptive fields of single neurones in the cat's
491   striate cortex. *J Physiol* **148,** 574-591 (1959).

492   16. Ohki, K., Chung, S., Ch'ng, Y.H. Kara, P. & Reid, R. Functional imaging with
493   cellular resolution reveals precise micro-architecture in visual cortex. *Nature*
494   **433,** 597-603 (2005).

495   17. Kondo, S. & Ohki, K. Laminar differences in the orientation selectivity of
496   geniculate afferents in mouse primary visual cortex. *Nat Neurosci* **19,**
497   316-319 (2016).

498   18. Kornhuber, H.H. & Deecke, L. Changes in the brain potential in voluntary
499   movements and passive movements in man: readiness potential and
500   reafferent potentials. *Pflugers Arch Gesamte Physiol Menschen Tiere* **284,**
501   1-17 (1965).

502   19. Libet, B., Gleason, C.A., Wright, E.W. & Pearl, D.K. Time of conscious
503   intention to act in relation to onset of cerebral activity (readiness-potential).
504   The unconscious initiation of a freely voluntary act. *Brain* **106,** 623-642
505   (1983).

506   20. Libet, B. Unconscious cerebral initiative and the role of conscious will in
507   voluntary action. *Behav Brain Sci* **8,** 529-566 (1985).

508   21. Zingg, B. et al. Neural networks of the mouse neocortex. *Cell* **156,**
509   1096-1111 (2014).

510   22. Sofroniew, N.J., Flickinger, D., King, J., & Svoboda, K. A large field of view
511   two-photon mesoscope with subcellular resolution for in vivo imaging. *Elife*
512   **5**, e14472 (2016).

513   23. Skocek, O. et al. High-speed volumetric imaging of neuronal activity in freely
514   moving rodents. *Nat Methods* **15**, 429-432 (2018).

515   24. Cong, L. et al. Rapid whole brain imaging of neural activity in freely behaving
516   larval zebrafish (*Danio rerio*). *Elife* **6**, e28158 (2017).

517   25. Kim, D.H. et al. Pan-neuronal calcium imaging with cellular resolution in
518   freely swimming zebrafish. Nat Methods 14, 1107-1114 (2017).

519   26. Coltman, J.W. The specification of imaging properties by response to a sine
520   wave input. *J Opt Soc Am* **44,** 468-471 (1954).

521   27. Mizuno, S. & Takada, T. Examination of Coltman's formula and rectangular
522   wave's response compared with sine wave's response. *Jpn J Radiol*
523   *Technol* **36,** 316-321 (1980).

28. Kobayashi, T., Yasuda, K. & Araki, M. Coordinated regulation of dorsal bone morphogenetic protein 4 and ventral Sonic hedgehog signaling specifies the dorso-ventral polarity in the optic vesicle and governs ocular morphogenesis through fibroblast growth factor 8 upregulation. *Dev Growth Differ* **52,** 351-363 (2010).

29. Tilly, B.C. et al. Histamine-H1-receptor-mediated phosphoinositide hydrolysis, Ca^{2+} signalling and membrane-potential oscillations in human HeLa carcinoma cells. *Biochem J* **266,** 235-243 (1990).

30. Mayford, M. et al. Control of memory formation through regulated expression of a CaMKII transgene. *Science* **274,** 1678-1683 (1996).

31. Sato, M. et al. Generation and imaging of transgenic mice that express G-CaMP7 under a tetracycline response element. *PLoS One* **10,** e0125354 (2015).

32. Manita, S. et al. A top-down cortical circuit for accurate sensory perception. *Neuron* **86,** 1304-1317 (2015).

33. Sato, M. et al. Fast varifocal two-photon microendoscope for imaging neuronal activity in the deep brain. *Biomed Opt Express* **8,** 4049-4060 (2017).

34. Butler, M.P. & Silver, R. Divergent photic thresholds in the non-image-forming visual system: entrainment, masking and pupillary light reflex. *Proc Biol Sci* **278,** 745-750 (2010).

35. Mohan, K. et al. Characterization of structure and function of the mouse retina using pattern electroretinography, pupil light reflex, and optical coherence tomography. *Vet Ophthalmol* **15,** 94-104 (2012).

36. Paxinos, G. & Watson, C. THE RAT BRAIN IN STEREOTACTIC COORDINATES. Academic Press: San Diego (1998).

37. Kobayashi, T. et al. Functional brain fluorescence plurimetry in rat by implantable concatenated CMOS imaging system. Functional brain fluorescence plurimetry in rat by implantable concatenated CMOS imaging system. *Biosens Bioelectron* **53,** 31-36 (2014).

38. Prusky, G.T., West, P.W. & Douglas, R.M. Behavioral assessment of visual acuity in mice and rats. *Vision Res* **40,** 2201-2209 (2000).

39. Dougherty, R. Extensions of DAMAS and benefits and limitations of deconvolution in beamforming. *11th AIAA/CEAS Aeroacoustics Conference*, AIAA 2005-2961 (2005).

40. Tribromoethanol (Avertin). *Cold Spring Harbor Protocols* **2006,** pdb.rec701

560   (2006).

561   41. Kawai, S., Takagi, Y., Kaneko, S. & Kurosawa T. Effect of three types of
562   mixed anesthetic agents alternate to ketamine in mice. *Exp Anim* **60,**
563   481-487 (2011).

564   42. Shibuki, K. et al. Dynamic imaging of somatosensory cortical activity in the
565   rat visualized by flavoprotein autofluorescence. *J Physiol* **549,** 919-927
566   (2003).

567   43. Zagha, E., Ge, X. & McCormick, D.A. Competing neural ensembles in motor
568   cortex gate goal-directed motor output. *Neuron* **88,** 565-577 (2015).

569   44. Komiyama, T. et al. Learning-related fine-scale specificity imaged in motor
570   cortex circuits of behaving mice. *Nature* **464,** 1182-1186 (2010).

571   45. Hira, R. et al. Spatiotemporal dynamics of functional clusters of neurons in
572   the mouse motor cortex during a voluntary movement. *J Neurosci* **33,**
573   1377-1390 (2013).

574   46. Li, N., Chen, T.W., Guo, Z.V., Gerfen, C.R. & Svoboda, K. A motor cortex
575   circuit for motor planning and movement. *Nature* **519,** 51-56 (2015).

576   47. Donchin, O. et al. Single-unit activity related to bimanual arm movements in
577   the primary and supplementary motor cortices. *J Neurophysiol* **88,**
578   3498-3517 (2002).

579   48. Cisek, P., Crammond, D.J. & Kalaska, J.F. Neural activity in primary motor
580   and dorsal premotor cortex in reaching tasks with the contralateral versus
581   ipsilateral arm. *J Neurophysiol* **89,** 922-942 (2003).

582   49. Verstynen, T., Diedrichsen, J., Albert, N., Aparichio, P. & Ivry, R.B. Ipsilateral
583   motor cortex activity during unimanual hand movements relates to task
584   complexity. *J Neurophysiol* **93,** 1209-1222 (2005).

585   50. Derosiere, G. et al. Similar scaling of contralateral and ipsilateral cortical
586   responses during graded unimanual force generation. *Neuroimage* **85,**
587   471-477 (2014).

588   51. Schultze-Kraft, M. et al. The point of no return in vetoing self-initiated
589   movements. *Proc Natl Acad Sci U S A* **113,** 1080-1085 (2016).

590   52. Kurata, K. & Tanji, J. Premotor cortex neurons in macaques: activity before
591   distal and proximal forelimb movements. *J Neurosci* **6,** 403-411 (1986).

592

593

594 **Figure legends**

595

596

597 **Figure 1** Wearable system for imaging the cerebral cortex in freely moving
598 animals

599

600 **(a)** Schematic image of the head-mounted laser camera (HLC) is shown. Right
601 photos show the HLCs for green (GFP) or red fluorescence (RFP) imaging.

602 **(b)** Schematic image of the HLC imaging system. The camera part is attached to
603 the spacer part when imaging is performed, and the head cap is attached to the
604 spacer part when the mouse is housing.

605 **(c)** The weight measurement of all the constituent parts of a typical HLC is
606 shown in the left image. Freely moving mice equipped with a single or dual
607 HLC's are shown in the right column images (Supplementary Movie 1).

608 **(d)** Fluorescence Ca^{2+} imaging of the occipital cortical area including the visual
609 cortex on an awake CaMK2a-G-CaMP mouse using the HLC (see also
610 Supplementary Movie 2). The left image is a representative single frame of the
611 movie. The middle image is a magnified view of the inset in the left image. The
612 right image is a representative frame of the subtracted imaging movie, which
613 was made by subtracting the average of the FI of each pixel from the FI of the
614 same pixel during the first 10 frames of the imaging movie. The HLC can
615 visualize excitatory neuronal activity as blinking light spots, and also visualize
616 the spatial distribution of fine capillaries with a wide field of view (4.25 x 5.66
617 mm). The view area of the HLC is adjustable. Bar indicates 1 mm.

618

619

620 **Figure 2** Optical specifications and adjustments of the HLC

621

622 **(a, b)** A checkerboard-design chart was captured by the HLC using different
623 fields of view. All results are shown in (b), using the representative images
624 shown in order of size of view from (a). The red line in (b) indicates an
625 approximate curve, expressed by $Y = -1.62 \times 10^{-2}X^2 + 9.4X - 0.48$, and the
626 correlation coefficient is $R^2 = 0.999$.

627 **(c)** Apparatus used for measuring a line-spread function (LSF) of the HLC using
628 a line chart. The red square indicates the view area of the HLC.

629 **(d)** The upper picture shows the image of the line chart taken by the HLC, and

630 the lower graph indicates the LSF (ordinate, light intensity; abscissa, vertical
631 position of the image). The red line corresponds to the position of the red lines in
632 (e, f).
633 **(e, f)** A square wave response function (SWRF) was calculated based on the
634 LSF (e) (lp = line pair, for a detailed calculation process see Methods section). A
635 modulation transfer function (MTF) was calculated based on the SWRF (f). The
636 horizontal and vertical red lines were drawn to cross at the point where the
637 SWRF = 0.03.
638 **(g)** Schematic image representing the light shape measurements. Several types
639 of light-shaping diffusers (LSDs) were attached in front of the white LED or LD at
640 a distance of 1 mm.
641 **(h)** The distributions of illumination by an LD, whose original beam divergence
642 was 3.3 x 14 deg at 40 mA, are shown as an 8-bit pseudo-colored image. The
643 distributions of illumination by a white LED are shown as controls. Numbers at
644 the top of the images show the LSD characteristics. Images are arranged
645 according to the order of deviation of the LSD from the circle to the horizontal
646 ellipse. Red squares indicate the typical view area of the HLC (4.0 x 5.3 mm).
647
648
649 **Figure 3** The HLC can acquire the fluorescence signal of the beads implanted
650 into the deep layers of the cerebral cortex
651
652 **(a)** Fluorescent beads were implanted into the mouse cortex after a craniotomy.
653 The blue circle and red square indicate the spacer position and the imaging area
654 of the HLC, respectively.
655 **(b, c)** Fluorescence images taken by a fluorescence stereo microscope (b) and
656 the HLC (c). Red arrows indicate the positions of implanted 15-μm beads, and
657 the numbers indicate the depth of implantation. Bar indicates 1 mm.
658 **(d)** In the two left images, the size and position of (b) and (c) were aligned based
659 on the pattern of blood vessels and the central position of the beads implanted at
660 a depth of 100 μm (red lines). White arrowheads indicate the bead positions.
661 The right two rows of 10 images show the magnified images of each bead taken
662 by the stereo microscope (Mic., left column) or the HLC (right column). The
663 vertical (v) and horizontal (h) rectangles were drawn to cross at the center of
664 each bead.
665 **(e)** Fluorescence intensity (FI) distribution along the (v) and (h) in (d) were

666   measured, and the relative FIs against averaged FI at the center of the bead at a
667   100-μm depth are shown.

668   **(f)** A summary of (e) is shown. The image size of the fluorescent beads was
669   calculated according to the number of pixels in the image. By comparing the FI
670   at the centers and perimeters of each light spot, the number of pixels of > 50% FI
671   and > 90% FI were counted. In the graph, error bars indicate the standard
672   deviation. Note that the values > 90% of the HLC stay almost invariant
673   regardless of depth (red line).

674

675

676   **Figure 4** The HLC visualized intracellular Ca^{2+} dynamics of individual cells in a
677   3D culture, and evoked neuronal activity in the deep layers of cerebral cortex

678

679   **(a)** Schematic image of the *in vitro* experiment. The sheet of 3D cultured Hela
680   cells transfected with the G-CaMP6 gene was placed into a glass bottom dish,
681   and Ca^{2+} imaging was performed with the HLC. Brightfield and fluorescence
682   images were taken by a stereomicroscope or the HLC. The transfected cells
683   emitted green fluorescence and were distributed sparsely across various depths.
684   Bar indicates 1 mm.

685   **(b)** The graph shows the changes in FI of a single cell. The FI increased after
686   histamine administration (+His), and then decreased when a solution of EGTA
687   was applied. The black line indicates the mean FI for each of 5 frames.

688   **(c)** Schematic diagram for the *in vivo* experiment. An electrode was inserted into
689   the cortex of a Thy1-G-CaMP7 mouse from the side after craniotomy. Then, the
690   HLC was applied to the cortex and Ca^{2+} imaging was performed.

691   **(d)** Pseudo-color images are shown for the change in FI before and after
692   electrical tetanic stimulation that was applied by an inserted electrode (see
693   Supplementary Fig. 6c for more detail). Bar indicates 1 mm.

694

695

696   **Figure 5** Zoom-up Ca^{2+} Imaging by using the HLC with short spacer in the freely
697   moving mice

698

699   The field-of-view size by the HLC can be changed for zooming up by twisting
700   the lens barrel. For small field of view with short working distance after zooming
701   up, it is preferable to use short spacer apparatus.

(a) Schematic images of different type of spacer are shown. The spacer part can be manufactured arbitrarily by changing its design.

(b) After imaging, the field-of-view size was confirmed by capturing the image of the reference chart.

(c) The images of the reference chart captured by the HLC with long or short spacer are shown.

(d) Ca^{2+} imaging was performed at the visual cortex of the CaMK2a-G-CaMP7 mouse by the HLC with the short spacer under the freely moving condition. The maximized fluorescence image of 20 fps movie for 5 min is shown at the left panel, and its magnified, maximized fluorescence image of the inset part of the left panel for 20 sec is shown on the right panel. Magenta arrowheads and numbers indicate the ROIs of which the light spots were randomly selected. The averaged and maximized movie in each 5 frames is shown in Supplementary Movie 7.

(e) The change rates of the fluorescence intensity ($\Delta F/F$) at each ROIs of (d) are shown.

Figure 6 Separation and identification of superimposed signals of individual cells by NMF in the HLC image

(a) Ca^{2+} imaging of the CaMK2a-G-CaMP7 mouse at the visual cortex was performed under the freely moving condition. The Maximized fluorescence image at 20 fps for 20 sec at the same view point as in Fig. 5d is shown.

(b) shows the subtracted maximized image of the movie.

(c) Using the raw 20 fps imaging data for 20 sec (total 400 frames), it was possible to segment the image into individual ROIs (region of interest) representing cell bodies by using a NMF algorithm (Methods section). The result is shown in (c), which shows the boundaries of 685 detected cells, plotted with different colors. It can be noted that many cells with spatial overlap were detected.

(d) shows the signal extracted by NMF for each cell over time, showing spontaneous activities of cells during free moving. With the application of the NMF algorithm, baseline removal and separation of temporal signals corrupted by spatial overlap of cells was achieved.

(e) shows the centroid locations of the cell bodies in X-Z plane, where X is the

longer image axis of (a) and Z is the depth of cortex corresponding to baseline value of the cell signal. Blue Roman numerals at the Z axis indicate the estimated cortical layer, assuming that deepest signal came from a depth of 1 mm. The broken blue line indicates the imaginary inclined cortical surface.

(f) The left image shows the centroid locations of the cells in three-dimension, where X and Z axis are same as (e), while Y-axis corresponds to the shorter image axis of (a). A three dimensional distribution of the cell bodies shows the presence of cells with various depths. The right image shows the same three dimensional distributions of the cell bodies with cell boundaries showed instead of centroid.

Figure 7 Observation of the physiological responses of individual neurons by large-scale imaging including the whole visual area of the cortex

(a) The left picture shows the experimental setup. The middle schematic diagram shows the HLC imaging area (red square, 4.25 x 5.66 mm) with the map of the brain area reconstructed from serial sections of the brain atlas (Supplementary Fig. 8a). Abbreviations: V1/2, primary/secondary visual cortex; PPC (PtA), posterior parietal cortex (parietal association cortex); S1 (Tr/BF)/S2, primary (trunk/olfactory barrel field)/secondary somatosensory cortex; M1/2, primary/secondary motor cortex. The right image is the deconvoluted fluorescence image of the occipital cortex in the awake CaMK2a-G-CaMP7 mouse taken by the HLC (see Methods section for detail). The lower four images are fluorescence images of the occipital cortex. Magenta and white arrowheads indicate the region of interests (ROIs) or negative control ROIs, and their $\Delta F/F$ are presented in (b), (c).

(b, c) The left and right graph shows the raw or averaged $\Delta F/F$ after a single (b) and 10x repeated flashlight stimulus (c), respectively, was applied by the LED. Gray vertical lines and red dots in each graph indicate the stimulation points. The red bold line data in the right graph of (b) and (c) indicate the means of 3 and 5 frames, respectively. Black lines mean negative control ROIs.

(d) Drifting gratings in 8 different directions were presented. The upper and lower graphs show the raw or averaged $\Delta F/F$. Examples of the specific $\Delta F/F$ increases according to the opposite degree stimulation (asterisks) are shown. Data indicated by the black line indicate the ROI of the negative control, and the

774   gray shaded time windows in each graph indicate the stimulation periods. The

775   red bold line data in the lower graphs indicate the means of 5 frames.

776   **(e)** Fluorescence image shows the ROIs of the #2 mouse. White arrowheads

777   indicate negative control ROIs, and green and magenta arrowheads show ROIs

778   for left graph or right graph in (d).

779   **(f)** shows the distribution of the ROIs of different orientation specificity by

780   different pseudo-colors in the same area as (e). See Methods for details.

781   **(g)** shows the selected ROIs with high level of orientation specific responses (top

782   3.5 %) among the ROIs in the same area as (e). See Methods for details. These

783   ROIs are mostly contained in the visual area of the cortex. Abbreviations: V1m/b,

784   primary visual cortex monocular/binocular zone; A, anterior; AM, anteromedial;

785   PM, posteromedial; RL, rostrolateral; AL, anterolateral; LM, lateromedial; LI,

786   laterointermediate; POR, postrhinal; P, posterior area.

787

788

789   **Figure 8** Imaging of the entire motor cortex reveals premotor activity

790

791   **(a)** The whole view of the restricted-motion experiment apparatus for mice.

792   **(b)** Hindleg movements (kicks) of the mouse were captured by web cameras

793   from both lateral sides of the apparatus.

794   **(c)** Schematic diagram showing classification of the periods during the

795   experiment. The movement state was subdivided into 3-sec durations

796   representing "Before" and "After" the initiation of motion. "Interphase" indicates

797   the 6-sec static state.

798   **(d)** Schematic image showing the HLC imaging position (red square). The Ca^{2+}

799   imaging was performed in awake CaMK2a-G-CaMP7 mice.

800   **(e)** The upper or lower row images show the results of the Ca^{2+} imaging with left

801   or right hindleg kicking, respectively. The left column images represent the

802   fluorescence images in which all raw-imaging data frames in 11 or 10-time left or

803   right kicks during the 6-sec motion state were merged into one frame by

804   maximization. Similarly, imaging data of the "interphase" state in 3-time left or

805   right kicks were merged, and the results are shown in the middle column by blue

806   pseudo-coloring. Also, "before" and "after" states are shown in green and red,

807   respectively. The right column images show the subtracted results, in which

808   green and red represent the ["before" − "interphase"] and ["after" − "interphase"]

809   of the middle column images, respectively. To make visual understanding easier,

810   the light spots of the subtracted images were enlarged and made brighter.

811   **(f)** The subtracted results of (e) for the spots with ΔF/F > 5% were plotted
812   spatiotemporally for each left or right kick (Supplementary Fig. 9c). The
813   brightness of each pseudo-colored dot represents an averaged frequency of
814   appearance of the peak in each trial.

815   **(g)** A schematic diagram summarizing the results in Fig. 8 and Supplementary
816   Fig. 9 for the left hindleg movement. The width and height of the half columns in
817   each hemisphere represent the number and the averaged activity of the "before-"
818   and "after-group" defined in Supplementary Fig. 9d-g. The before-group neurons,
819   which have a peak excitation frequency before the initiation of movement,
820   continue to show lateralized distribution and activity both before and after the
821   motion, while the after-group neurons show less lateralization.

822

823

Methods

Development and construction of a wearable imaging system

The wearable HLC imaging system is composed of two major parts, the camera and the spacer (Fig. 1a). The two parts can be separated or combined by using the O-ring as a fastener hooked on their side protrusions. The cylindrical spacer body has a cranial imaging window (object plate) at its base that makes direct contact with the surface of the cortex. The spacer is attached to the mouse head, and the camera is combined with the spacer when imaging is performed. The detachable wearable camera helps with the long-term housing of experimental mice by keeping them free from movement restriction by an electrical wire (Supplementary Movie 1). The camera module (DCT, Co., Japan) has a CMOS (complementary metal-oxide semiconductor) image sensor chip (1/13", 480 x 640 pixels, pixel size = 1.75 x 1.75 μm; OmniVision Technologies Inc., USA) and a deep-focus optical system. The imaging area is adjustable, and the bottom diameter of the typical cylindrical spacer body is 7.5 ± 0.5 mm. Although the design of spacer body is changeable, typically the height of the spacer body is 9.0 ± 0.5 mm (long spacer in Fig. 5), in this case, the volume of spacer part is approximately 500 mm^3. The thickness of head cap and gasket is 1.0 mm ± 0.5 mm each, therefore, the total volume of the HLC is approximately 600 mm^3. The HLC is lightweight (typically 0.9 g) and does not disturb the natural behavior of a small mouse such as individuals from the C57BL/6 line (Supplementary Fig. 2d, e).

The HLC has an LD for the excitation light and an absorption filter for the emission light. The camera was constructed by firmly attaching the micro camera and LD to the head cap with epoxy resin. For green and red fluorescence imaging, the high pass absorption filter set at > 500 or > 520 and > 560 or > 580 nm, respectively (Fujifilm, Co., Japan) was attached in front of the lens, and a blue or green LD (450-460, 488 or 530 nm; OSRAM, Co., Germany) was used, respectively. The LD along with the LSD (Optical Solutions, Co., Japan) and the copper heat sink is driven by the LD driver (Supplementary Fig. 4a, b). The glass object plate (0.525 mm thickness; Matsunami Glass Ind., Ltd., Japan) was firmly attached to the bottom of the spacer body. The head cap and the spacer body were made based on 3D-CAD data by cutting an acrylic plate with a lathe machine.

860   The image data were transferred to a computer via a USB cable, displayed
861   on a monitor, and saved as an AVI movie file using free software, AmCap
862   (Microsoft, Co., USA). For Ca^{2+} imaging, the image sensor was typically driven
863   at < 30 fps to ensure sufficient sensitivity, stable data transfer and preservation,
864   and real-time presentation on the monitor. The ΔF/F of the mechanical noise
865   when measuring inorganic matter was below the detection limit of 8-bit data.
866   ImageJ (supplied by the National Institutes of Health, USA) was used for all
867   image data analysis. Graphic art works were performed using the free software,
868   DesignSpark Mechanical (3D CAD; computer-aided design, Radiospares
869   Components, Inc.) and GIMP (GNU Image manipulation program, Free Software
870   Foundation, Inc.).

871

872   Verifying the optical specifications of the HLC

873

874   The HLC has deep-focus optics and its working distance (WD) can vary by
875   adjusting the lens barrel. The lens position change can also vary with the field of
876   view size at the same time. When the lens barrel is twisted and pulled out for a
877   short WD, the view field becomes small. In contrast, when the lens barrel is
878   twisted and pressed for a long WD, the view field becomes large. If the position
879   of the camera is adjusted properly such that the WD fits the object, the HLC can
880   obtain either a narrow or wide field of view arbitrarily, as shown in Fig. 2a, b. The
881   minimum field of vision is 2.00 x 2.67 mm at 2.70 mm of WD, and here the
882   maximum resolution was 8.33 µm/lp (line pair), 4.17 µm/pixel. The maximum
883   field of vision is 10.0 x 13.3 mm at 15.0 mm of WD, and here the minimum
884   resolution was 41.7 µm/lp, 20.8 µm/pixel.
885   There is a physical limit to the barrel adjustment range, and if adjusted to an
886   extreme WD value, light aberration cannot be corrected and the peripheral
887   portion of the image is distorted in a pincushion pattern. For instance, with 6.65 x
888   8.87 mm imaging, the central part of the image can cover 6.65 mm vertically,
889   whereas that of the periphery vertically covers 6.40 mm, which means DTV
890   (television distortion) = (6.65 − 6.40)/6.40 x 100 = 3.91 [%]. Additionally, the
891   central and peripheral parts of the image horizontally cover 8.86 and 8.67 mm,
892   respectively. Therefore, the optical distortion is 2.78 %, calculated as follows:
893   distortion [%] = [(actual half diagonal distance) − (predicted half diagonal
894   distance)]/(predicted half diagonal distance) x 100 = $\sqrt{[(6.65/2)^2+(8.86/2)^2]}$ -
895   $\sqrt{[(6.40/2)^2+(8.67/2)^2]}/\sqrt{[(6.40/2)^2+(8.67/2)^2]}$ x 100. The pincushion distortion will

896   be suitable for observing the convex cortex, but not the barrel distortion (see

897   also right panel in Supplementary Fig. 6b).

898   Next, the depth of field (DOF) was calculated. DOF is defined by an

899   associated resolution and contrast, and is estimated by a single value calculated

900   from the diffraction limit as a theoretical approximation; however, it is difficult to

901   make a genuine comparison because many imaging lenses are not diffraction

902   limited. Therefore, the only way to truly determine DOF is to use a test target.

903   Normally, even if a lens has infinite focus theoretically, the spatial resolution of

904   the image sensor (density of the photo-diode pixel array) is limiting for DOF.

905   Firstly, the line spread function (LSF) of the HLC in the case of 6.65 x 8.87 mm

906   imaging (resolution; 27.7 μm/lp, 13.9 μm/pixel) was analyzed by using a line

907   chart (Fig. 2c, d), and then based on the results of the LSF, the square wave

908   response function (SWRF) was calculated as follows:

$$C_{out}(u) = \frac{\frac{1}{2}\left(I_{\max}(u) - I_{\min}(u)\right)}{\frac{1}{2}\left(I_{\max}(u) + I_{\min}(u)\right)} = \frac{I_{\max}(u) - I_{\min}(u)}{I_{\max}(u) + I_{\min}(u)}$$

909

$$\mathrm{SWRF}(u) = \frac{C_{out}(u)}{C(0)} = \frac{\left[\frac{I_{\max}(u) - I_{\min}(u)}{I_{\max}(u) + I_{\min}(u)}\right]}{\left[\frac{I_{\max}(0) - I_{\min}(0)}{I_{\max}(0) + I_{\min}(0)}\right]}$$

910

911    $C_{out}(u)$ is the output contrast of rectangular wave pattern at spatial frequency u.

912   I_{max} and I_{min} are the values obtained by converting the intensity into the dose at

913   each square wave of the LSF. As a result, the SWRF is 24.7 [lp] at a cut-off point

914   of 0.03, as generally used by many optical manufacturers (Fig. 2e). That SWRF

915   value corresponds to the position at 600 pixels in LSF (Fig. 2d). In the line chart,

916   the line pair width is 0.912 mm. Therefore, DOF is 24.7 x 0.912 x √3/2 = 19.5

917   [mm].

918   Finally, to calculate an effective spatial frequency at the distorted edge of

919   the imaging field, the SWRF (a rectangular wave response function) was

920   corrected to the modulation transfer function (MTF; sine wave response

921   function), calculated with the correction via Coltman's formula[26]. MTF is a

922   measure of an imaging lens's ability to transfer contrast from the object plane to

923   the image plane at a specific resolution, and is expressed with respect to image

924   resolution (lp/mm) and contrast (%). Typically, as resolution increases, contrast

925 decreases until a cut-off point, at which the image becomes irresolvable and grey.
926 The formula is shown below.

$$\text{MTF}(u) = \frac{\pi}{4}\sum_{k=1}^{\infty} B_k \frac{\text{SWRF}\{(2k-1)u\}}{(2k-1)}$$

927

$$Resolution = \frac{1}{\text{lp/mm}} \times 1000$$

928

929 If the total number of prime numbers in ($2k$ - 1) is m and the number of types of
930 prime numbers is n, $Bk = 0$ when $m > n$, and $Bk = (-1)^n(-1)^{k-1}$ when $m = n$. For
931 the calculation of MTF, up to the fourth term of the expansion formula was used
932 according to a previous verification[27]. As a result, MTF resulted in an effective
933 spatial frequency of 15.5 lp/mm where MTF = 0.03 (Fig. 2f), producing an
934 effective spatial resolution of 64.5 μm/lp. Therefore, the estimated minimum
935 effective spatial resolution was 64.5 μm/lp at the distorted edge of the imaging
936 field, which is 2.3 times that of 27.7 μm/lp at the center of the visual field in the
937 case of 6.65 x 8.87 mm imaging (resolution; 27.7 μm/lp, 13.9 μm/pixel).
938 According to the above results, although actual measurement values will
939 fluctuate depending on the measuring environment and optical distortion, a
940 discriminable minimum light spot is presumed as approximately two times
941 blurred at the edge of the field of view due to natural optical aberration.

942

943 Quantitative imaging analysis using fluorescent beads

944

945   After craniotomy, fluorescent beads (F21010, green fluorescent
946 FluoSpheres, polystyrene; Thermo Fisher Scientific Inc., USA) were implanted
947 into the cortex of the anesthetized mice at different depths by using a needle and
948 micromanipulator (Fig. 3). The bead diameter of 15 μm was similar to the
949 general cell size. The stereomicroscope has a general objective focus lens,
950 whereas the HLC has a deep-focus lens. In Fig. 3, the field of view of the HLC is
951 3.80 x 5.06 mm, 1 pixel = 7.917 μm. A general objective lens can handle a bright
952 image because the F value is smaller than the deep-focus lens, and a sharper
953 image was obtained by focus imaging in Fig. 3b than in Fig. 3c; however, the
954 DOF was shallow. In contrast, with the HLC, the fluorescence derived from every
955 bead can be detected even at an 800 μm depth, suggesting that the detectability
956 of fluorescence by the deep-focus lens is apparently higher than that for a

957 conventional focus lens. In the left 2 images of Fig. 3d, the position of the upper
958 beads at 400 µm depth does not match exactly between the conventional
959 microscope and the HLC. This is likely due to differences in optical distortion.
960 Regarding the small 10 images to the right column in Fig. 3d, although these
961 images are shown brightly for the sake of convenience in aligning and
962 distinguishing shapes, the measurement was actually performed based on the
963 raw data, with the quantitative results shown as a graph in Fig. 3e, f. In the
964 microscope image, the FI and shape of each bead at the same depth are almost
965 the same (left graph in Fig. 3e), supporting the accuracy of the experimental
966 system. Thus, the deeper the position of the beads, the lower the FI becomes in
967 the image taken by the conventional stereomicroscope, until the FI is reduced
968 almost to background levels at 800 µm. In contrast, the decrease in FI with depth
969 is mild for the HLC imaging, and a stronger fluorescent signal than for the
970 conventional microscope was detected even at a depth of 800 µm. Compared at
971 the same depth, the bead's FI level and shape captured by the HLC are slightly
972 variable. This can be reasonably explained by distribution differences in the
973 excitation light (see also the image in Fig. 2h) and optical distortion (as
974 mentioned above in Methods section for Fig. 2a). In fact, from the center of the
975 field of view to the periphery, the intensity of the excitation light decreases and
976 the size increases. It is possible to correct the above-mentioned variability
977 mathematically, if necessary, in actual functional brain cellular imaging.
978 Concerning the result of Fig. 3f, the deeper the position of the bead, the larger it
979 becomes relative to its actual size in the conventional microscope images. In
980 contrast, image sizes with the HLC are generally constant relative to depth.
981 Specifically, the enlargement ratio at 50% FI with the stereomicroscope image
982 against the actual bead size is 4.10 (at 100 µm), 14.6 (at 400 µm), and 17.6 (at
983 800 µm), compared to 4.75 (at 100 µm), 5.80 (at 200 µm), and 6.86 (at 800 µm)
984 for the HLC imaging. Thus, both the decline in signal detection ability and the
985 expansion of the outline seem to be less when using the HLC due to the
986 deep-focus optics.
987
988 Ca^{2+} imaging in 3D culture cells
989
990   Cell cultures in 2D and 3D, gene transfection, and drug administration were
991 performed according to previous reports[9,28]. Hela cells, derived from a human
992 cervical cancer, were transfected with the G-CaMP6 gene[12] under 2D conditions.

After transfection, cells were embedded in the collagen gel as an extracellular matrix to imitate brain structure as a brain phantom. Hela cells are activated by histamine through the histamine H_1-receptor by producing intracellular Ca^{2+} increases[29]. Thus, when a histamine solution (final 5 µM) was applied to the dish, rising Ca^{2+} increases were detected by the HLC at 30 fps imaging (Supplementary Fig. 6a, Supplementary Movie 4). In contrast, the increase was abolished by 5 mM EGTA (Fig. 4b).

Animal studies

All procedures involving animals conformed to the animal care and experimentation guidelines of the RIKEN Animal Experiments Committee and Genetic Recombinant Experiment Safety Committee. C57BL/6J (SLC Co., Japan), CaMK2a-tTA (Jackson 3010)[30], TRE-G-CaMP7-2A-DsRed2[31], and Thy1-G-CaMP7-2A-DsRed2 (Thy1-G-CaMP7) [32,33] mice, aged 6-12 months, were used for the *in vivo* experiments (see details of surgical operation in Supplementary Fig. 1).

Cell detection and signal extraction

In Fig. 6c, imaging data analysis was performed using custom codes in LabVIEW (National Instruments) and Matlab (Mathworks). Brain imaging movies were processed in the following steps to detect cell bodies and extract their temporal signals. First, for each pixel of the image, a variance value was calculated using the time signal of that pixel. Thus a variance map was obtained for each movie. This variance map has peaks and valleys of various heights, corresponding to the location cell bodies. This variance map was then cut horizontally at different heights to obtain 100-200 slices, depending on the data. Each of these slices showed presence of segmented ROIs. Cells with weaker activation were visible in slices cut in higher depth from the top, while highly activated cells were found in slices in lower depths. All ROIs with area in the range of 30-150 squire microns were gathered to form a preliminary set of cell-like ROIs. For each ROI, a 2-pixel-wide Gaussian filter was used to smooth the spatial distribution of the ROI. However, as in many cases same cells were detected multiple times in varying depths, temporal correlations among these ROIs were checked. ROIs having temporal correlation value >0.9 and some

1029   degree of spatial correlation were considered as same cells, and they were
1030   added to form one single ROI. By performing this task recursively, we obtained a
1031   second set of ROIs representing the cell bodies in the movie.

1032   In the next step, we calculated temporal signals of these ROIs from the
1033   movie by taking weighted average of temporal signal of all the pixels in a specific
1034   ROI. As the intensity of the movie pixels varied due to position of pixels, ROIs
1035   has various levels of baseline intensity signals. Furthermore, in case of weakly
1036   activated cell bodies, actual calcium transient signal was not clearly visible due
1037   to temporally fluctuating baseline. Therefore, to eliminate baseline effect, we
1038   used a NMF (Non-negative Matrix Factorization) algorithm[14] to extract actual
1039   activation of the cells while separating the spatio-temporal baseline of the image
1040   simultaneously by solving the following problem:

$$Minimize: \; \| (F - W \times H - S_b \times A_b) \|_2$$

F : original image

W: spatial components corresponding to cells

H: temporal components corresponding to cells

S_b: Spatial baseline

A_b: Temporal baseline

1041   With the application of the above mentioned algorithm, baseline removal and
1042   separation of temporal signals corrupted by spatial overlap of cells was
1043   achieved.

1044

1045   Perceptual and behavioral tests

1046

1047   In Fig. 7, awake mice received either light stimulation or an 8-direction
1048   drifting grating with blue light stimulation using a light emitting diode (LED, peak
1049   wave length 470 nm; Stanley Electric Co., Ltd., Japan) driven by a function
1050   generator, or video stimulation using a computer monitor. C57BL/6 mice have
1051   high photosensitivity against blue light judging from their pupillary light reflex[34,35].
1052   Thus, to increase the stability of repeated visual inputs to the mouse, the head of
1053   the mouse was fixed with a stereotactic instrument while its body was allowed to
1054   move freely (upper left image in Fig. 7a), so that the left eye was given the visual
1055   stimuli while the right eye was masked. All experiments were done in a dark
1056   room, and the imaging was started after 15-minute habituation. In Fig. 7a, the
1057   upper middle schematic diagram for the rodent brain was drawn with partial
1058   modification by reconstructing the transverse sections of the brain atlas[36,37]

1059 (Supplementary Fig. 8a).

1060 A single flashlight stimulation (rectangular pulse 0.1 sec) or 10-times
1061 repeated flashlight stimulation (rectangular pulse trains of 0.5 sec, 20 Hz,
1062 duration 25 ms, interval 25 ms) were applied to the mouse. Similarly, the
1063 8-direction drifting grating (each drifting duration 3 sec, interval 6 sec, > 0.5
1064 cycle/degree[38]) was presented to the mouse. Ca^{2+} imaging was then performed
1065 using the HLC on the CaMK2a-tTA x TRE-G-CaMP7-2A-DsRed2 mice
1066 (CaMK2a-G-CaMP7) over the right visual cortical area. ROIs of 4 pixels were
1067 selected by visual judgment, and changes in FI were measured from the raw
1068 imaging data. Fig. 7b represents the results of 12 ROIs of 2 mice in 6 trials, while
1069 Fig. 7c shows the results of 7 ROIs of 2 mice in 3 trials. All ROI positions are
1070 shown in the lower column images of Fig. 7a. In Fig. 7d, the left and right graphs
1071 plot the raw values obtained from 15 ROIs of 2 mice in 3 trials and 12 ROIs of 2
1072 mice in 1 trial, respectively. ROIs of one mouse (ID: #2) among 2 mice is
1073 exemplified in Fig. 7e. In Fig. 7f, Data of 4 opposite angles ([0 and 180°], [45 and
1074 225°], [90 and 270°], and [135 and 315°]) during the 3-second stimulation were
1075 maximized, and data of right angles were subtracted as below, ΔF [0 and 180°] =
1076 FI ([0 and 180°] – [90 and 270°]), ΔF [45 and 225°] = FI ([45 and 225°] – [135
1077 and 315°]), ΔF [90 and 270°] = FI ([90 and 270°] – [0 and 180°]), ΔF [135 and
1078 315°] = FI ([135 and 315°] – [45 and 225°]). Finally, these four different ΔF's
1079 were assigned with different 4 colors (Green, Blue, Magenta, Yellow), and each
1080 ROI was given a pseudo-color by weighed superimposition of these 4 colors to
1081 represent the orientation preference of each ROI (Fig. 7f). Among these ROIs,
1082 those with top 3.5 % of pseudo-color intensity are presented in Fig. 7g.

1083 Regarding deconvolution (upper right image in Fig. 7a), diffraction point
1084 spread functions and iterative deconvolutions were calculated according to
1085 Dougherty's algorithm[39]. In the present study, FI measurements were always
1086 extracted from raw data, and not from the deconvoluted data.

1087 For the maximum points extraction (Supplementary Fig. 3), light points were
1088 selected and counted from the image after subtraction of background with the
1089 parameter of a noise tolerance of 10 according to the ImageJ algorithm
1090 constructed by Michael Schmid (NIH, USA).

1091

1092 For the "restriction motion experiment" represented in Fig. 8, an apparatus
1093 was made to analyze neuronal activity in the mice derived from specific
1094 voluntary movement initiation. A cylindrical restraint tube was filled with urethane

1095 foam resin to fit the body shape of the mouse, and its external wall was painted
1096 with black ink. Hence, the body of the mouse is held firmly when it is inserted in
1097 the tube, and other parts of the body except the legs do not move as much, thus
1098 mildly restricting the mouse motion and sensation. Before beginning the
1099 measurements, the mouse was placed in the cylindrical restraint and their legs
1100 protruding from the tube were attached to splints, which functioned as
1101 body-worn foot levers. The splints could move according to the leg motions or
1102 could be made immovable individually by the fixing of bolts. The motion of the
1103 splint was followed by the movement of a line drawn outside the splint and
1104 captured by a web camera at 30 fps from both lateral sides. Then, Ca^{2+} imaging
1105 was performed after 15-minute habituation in 4 mice (ID: #3-6) using an HLC
1106 attached to the spacer protruding from the upper part of the restraint tube, at 20
1107 fps (Fig. 8) or 10 fps (Supplementary Fig. 9a, Supplementary Movie 9).

1108   A series of analyses comprising a "comprehensive quantitative analysis"
1109 (Fig. 8e, f, Supplementary Fig. 9b, c) and an "overall qualitative analysis"
1110 (Supplementary Fig. 9d-g) were also conducted as described in the respective
1111 figure legends. The maximization of FI in the imaging data, described as a
1112 maximum intensity projection in Supplementary Fig. 7, removed the basal
1113 random noise similarly to an averaging process, but without losing the
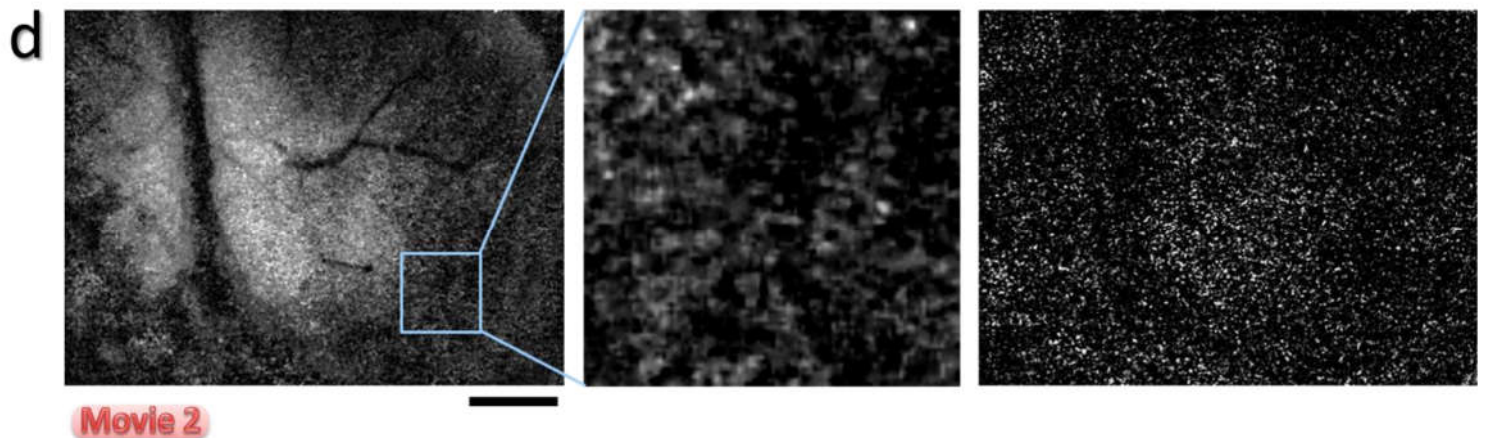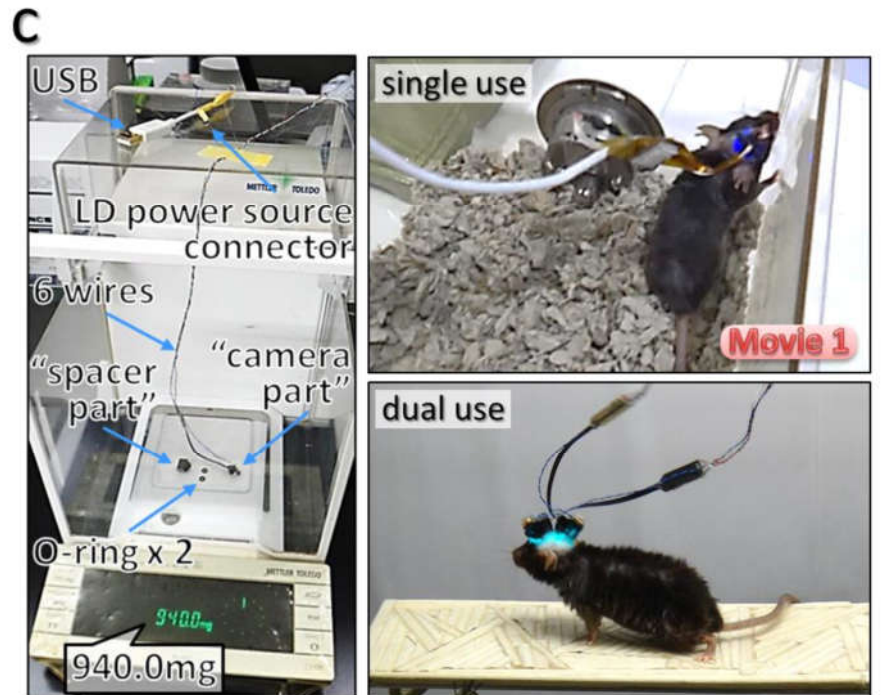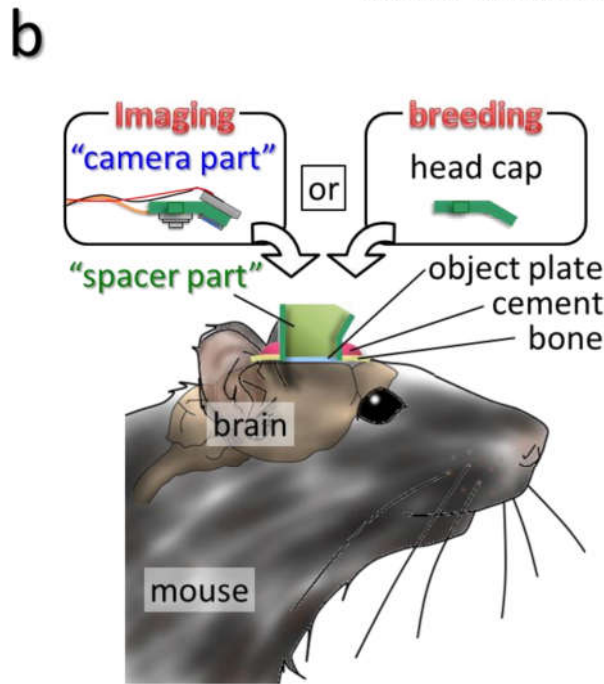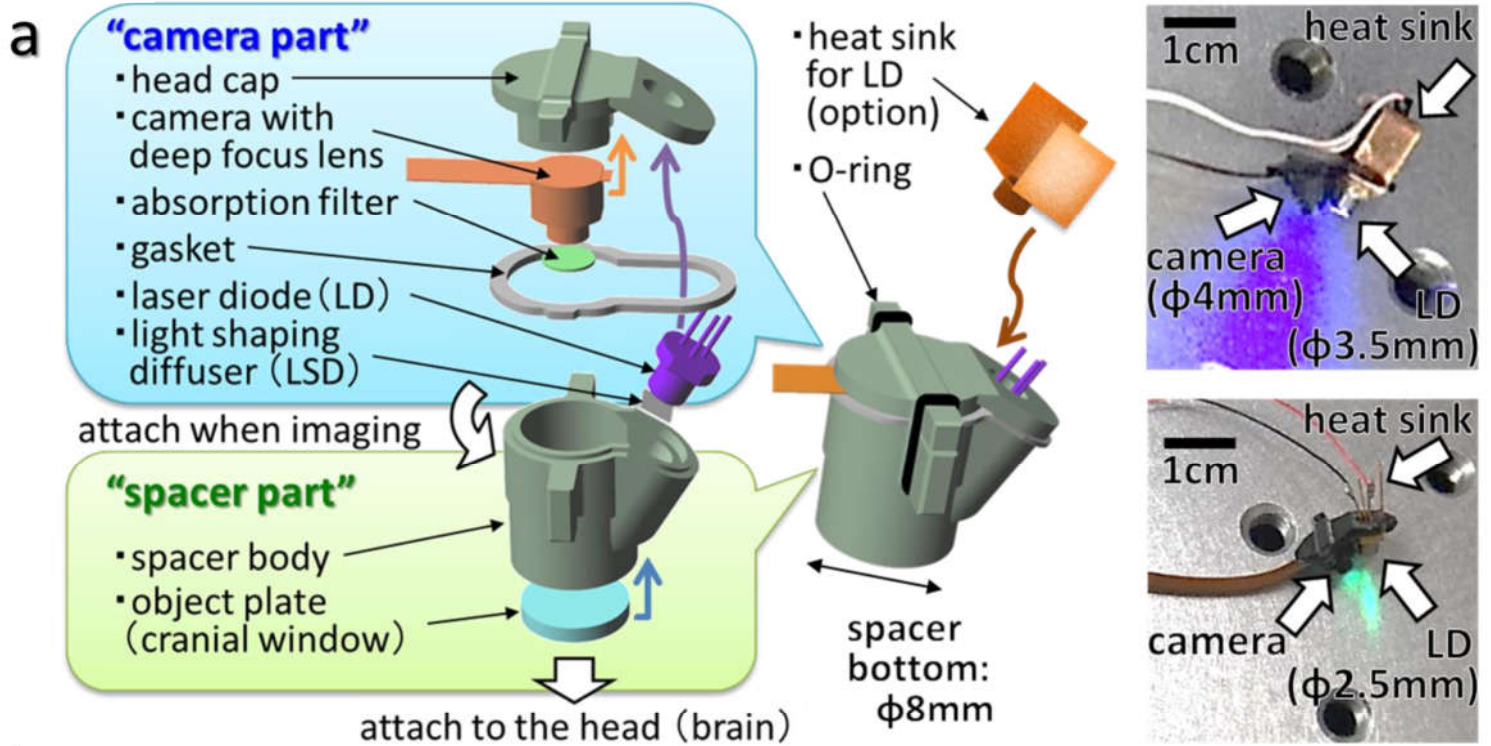1114 information of relatively rare but important events.
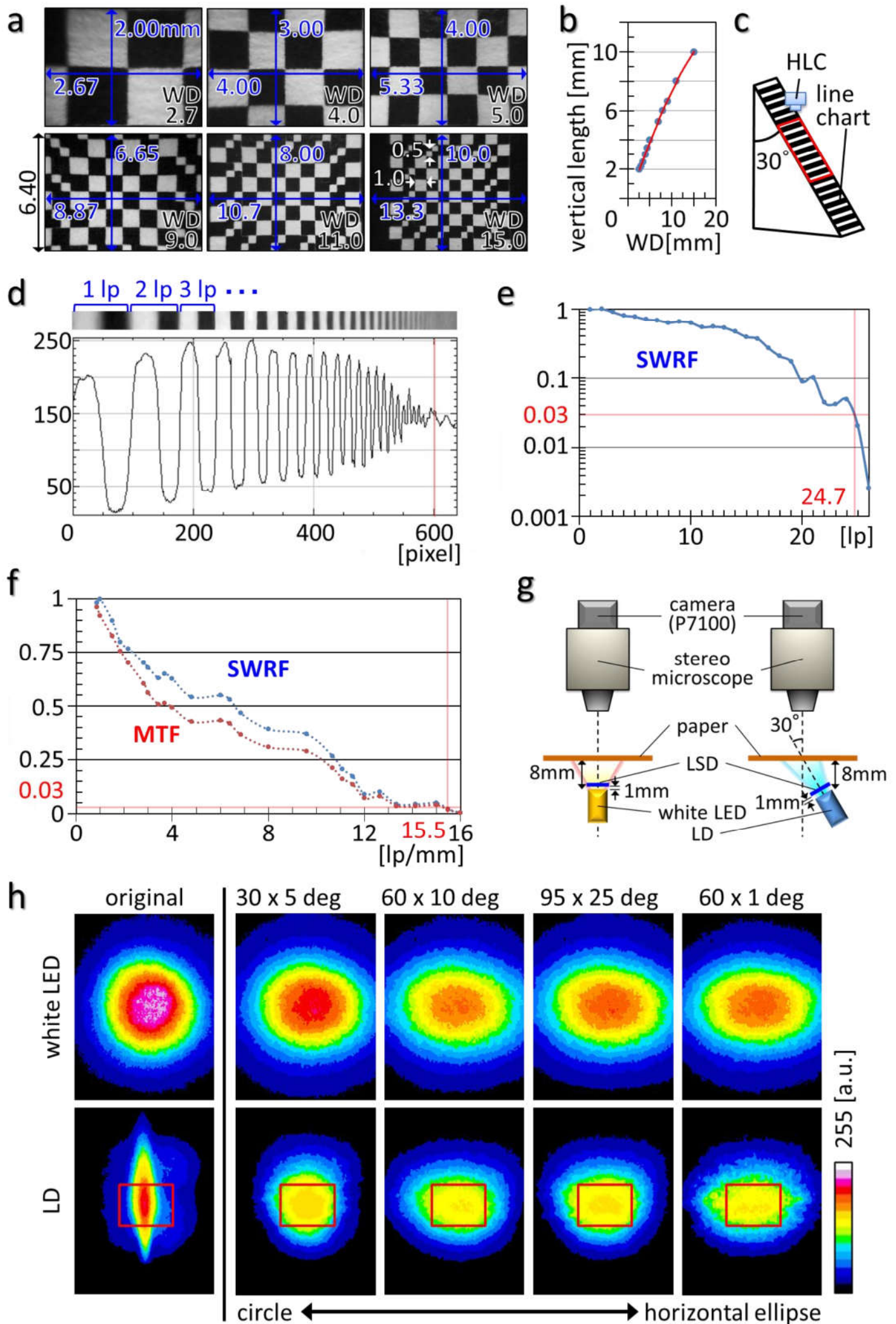
1115

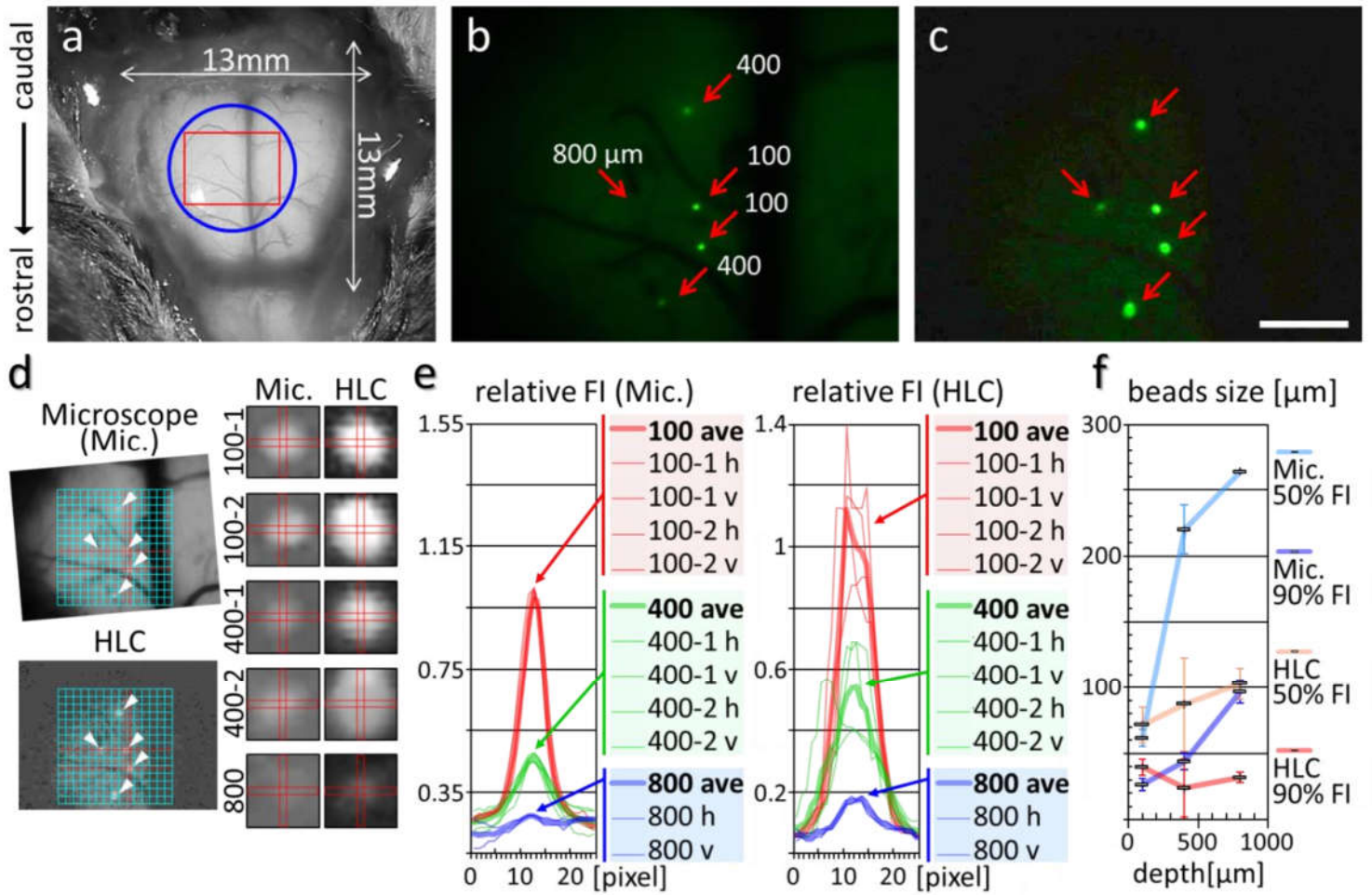1116 **Data availability**
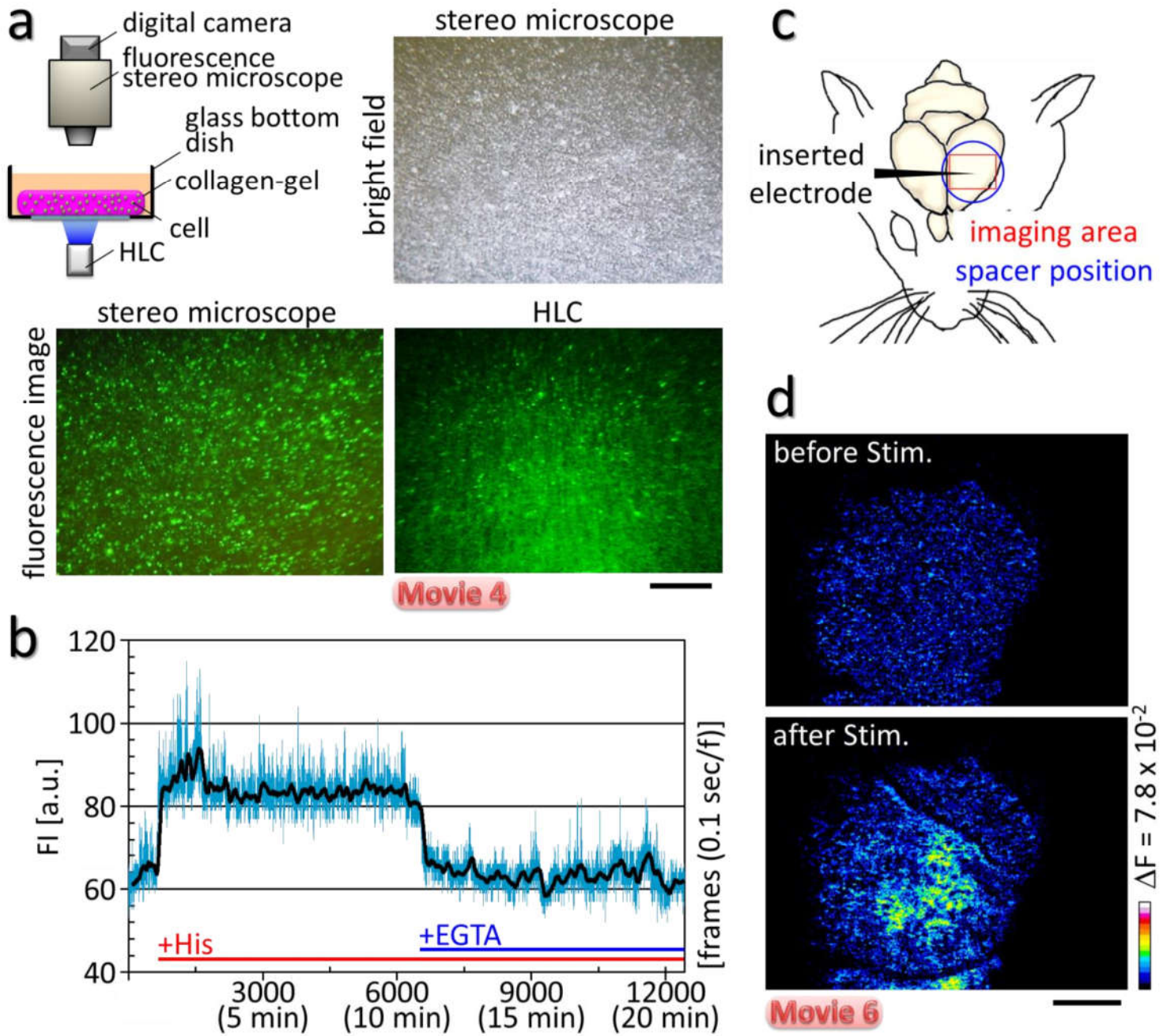
1117

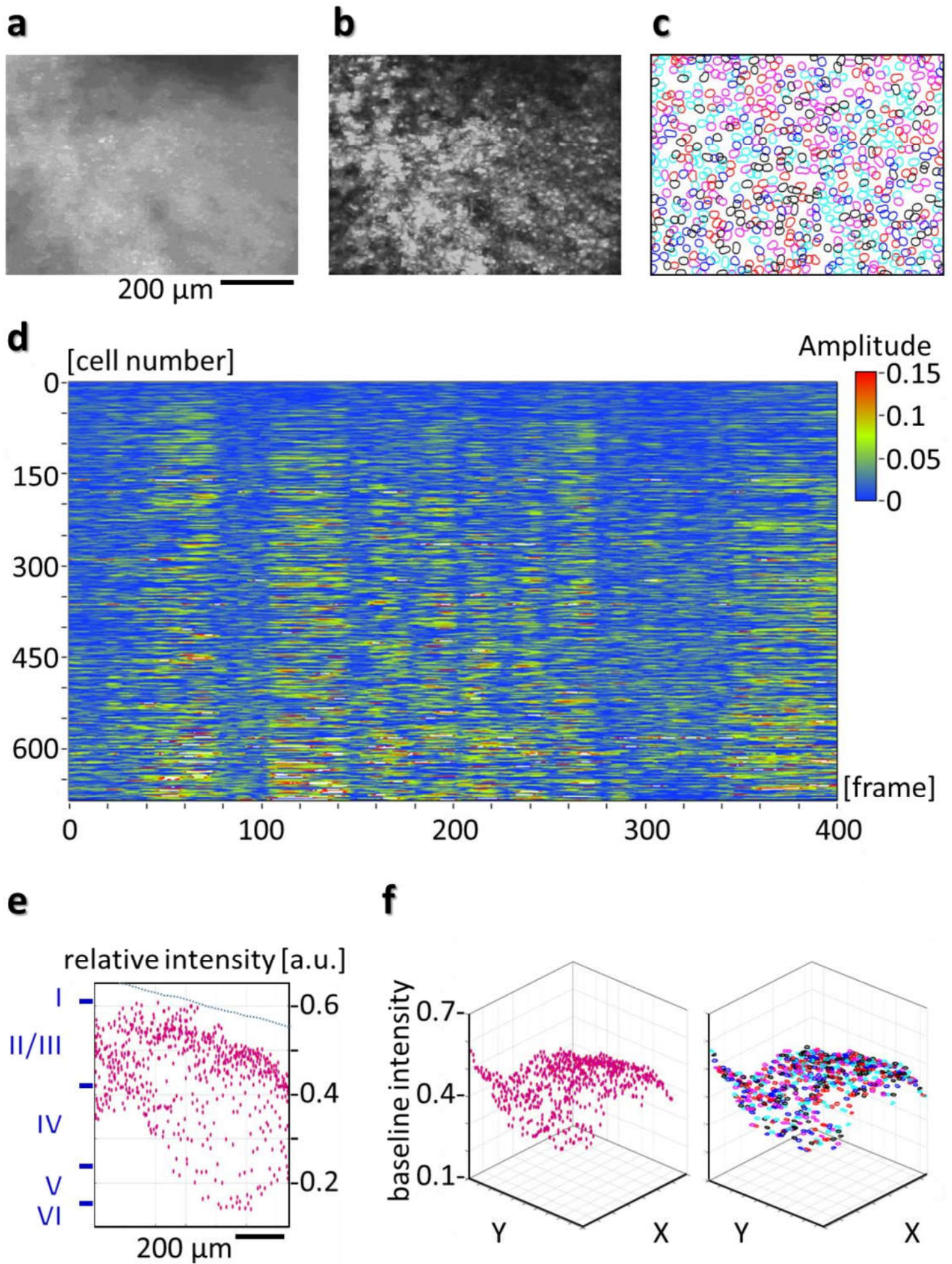1118 All relevant data are available from the authors.

1119

Fig. 1

Fig. 2

Fig. 3

Fig. 4

Fig. 5

Fig. 6

a

b

c

200 µm

d

[cell number]

Amplitude

[frame]

e

relative intensity [a.u.]
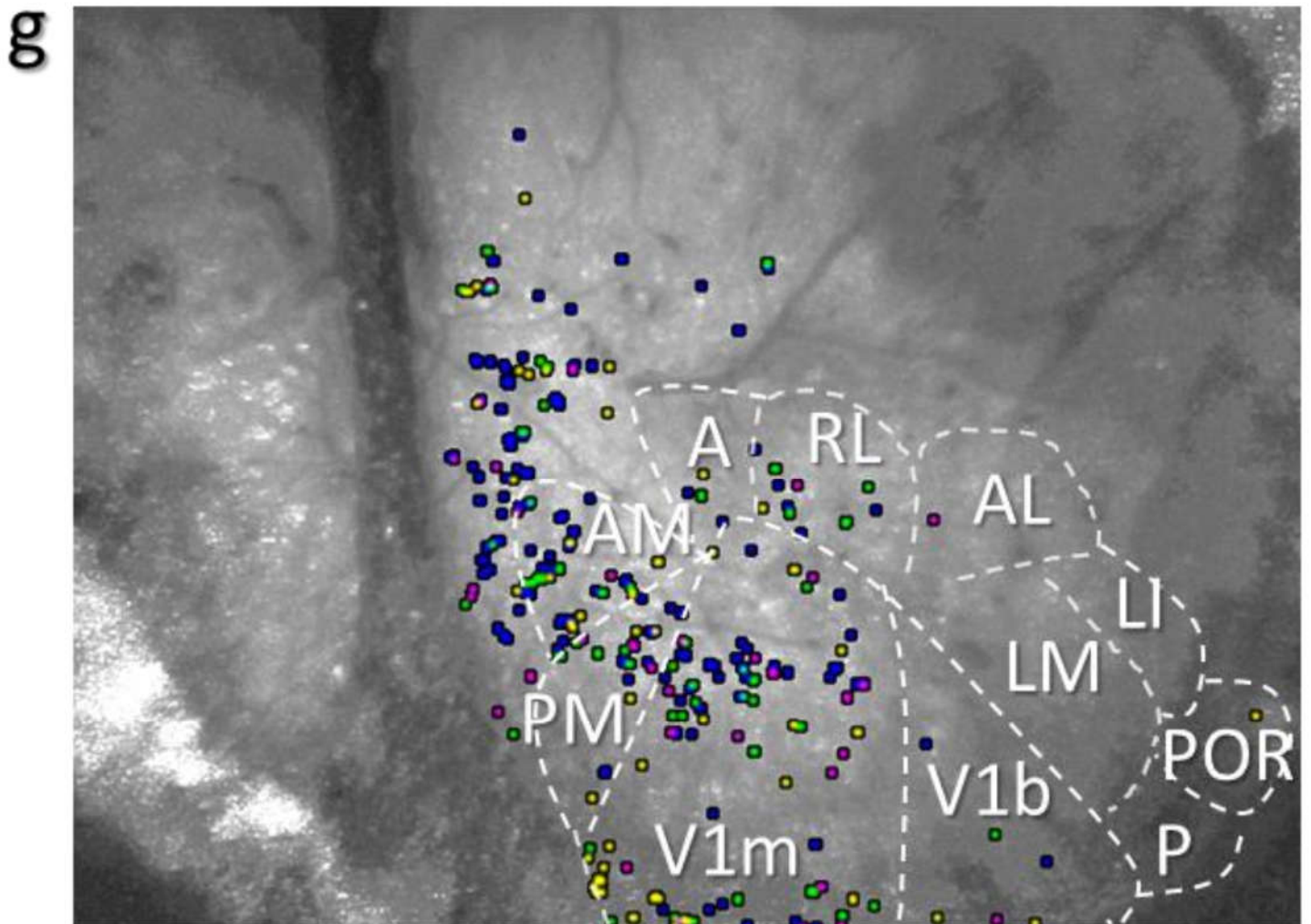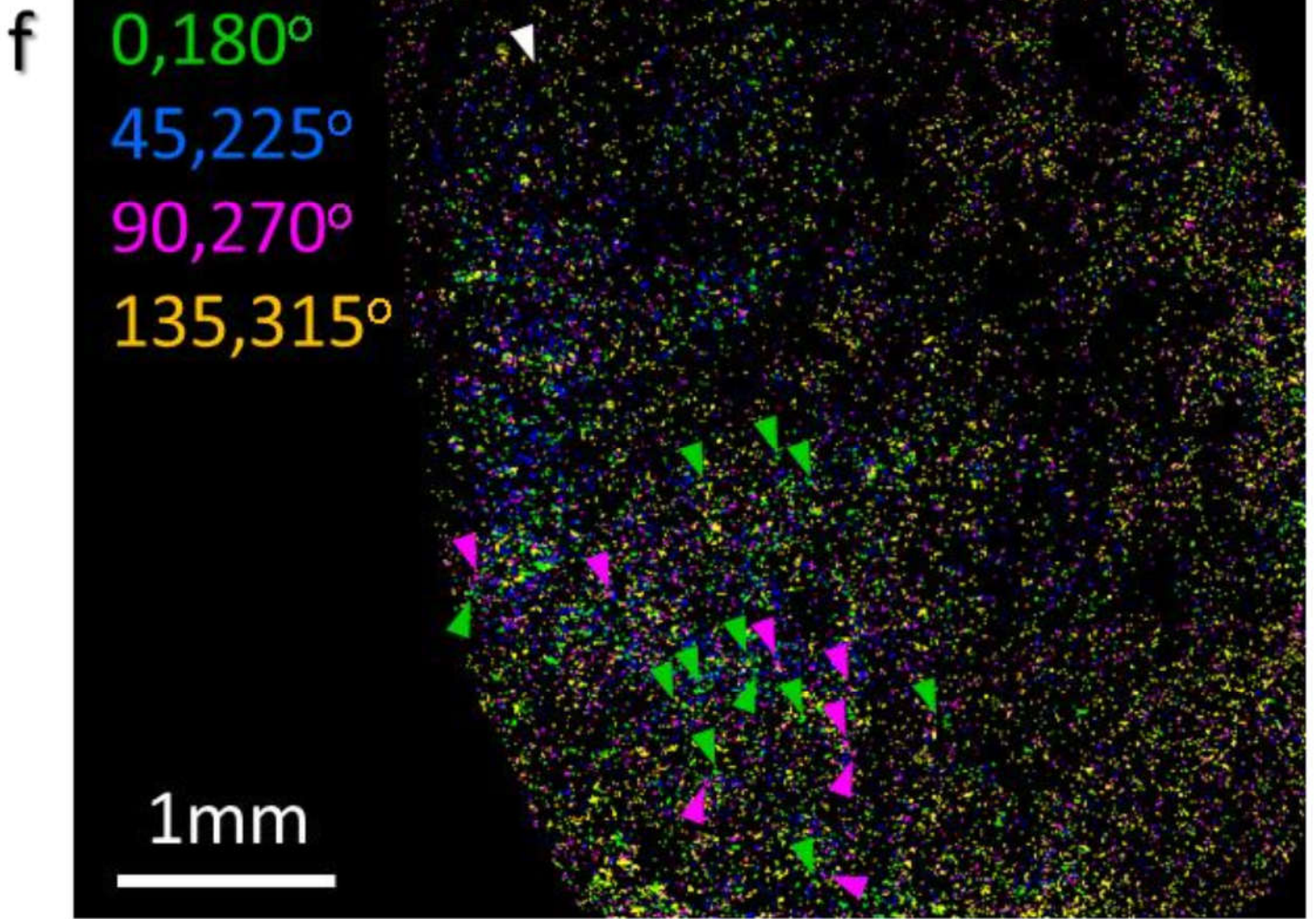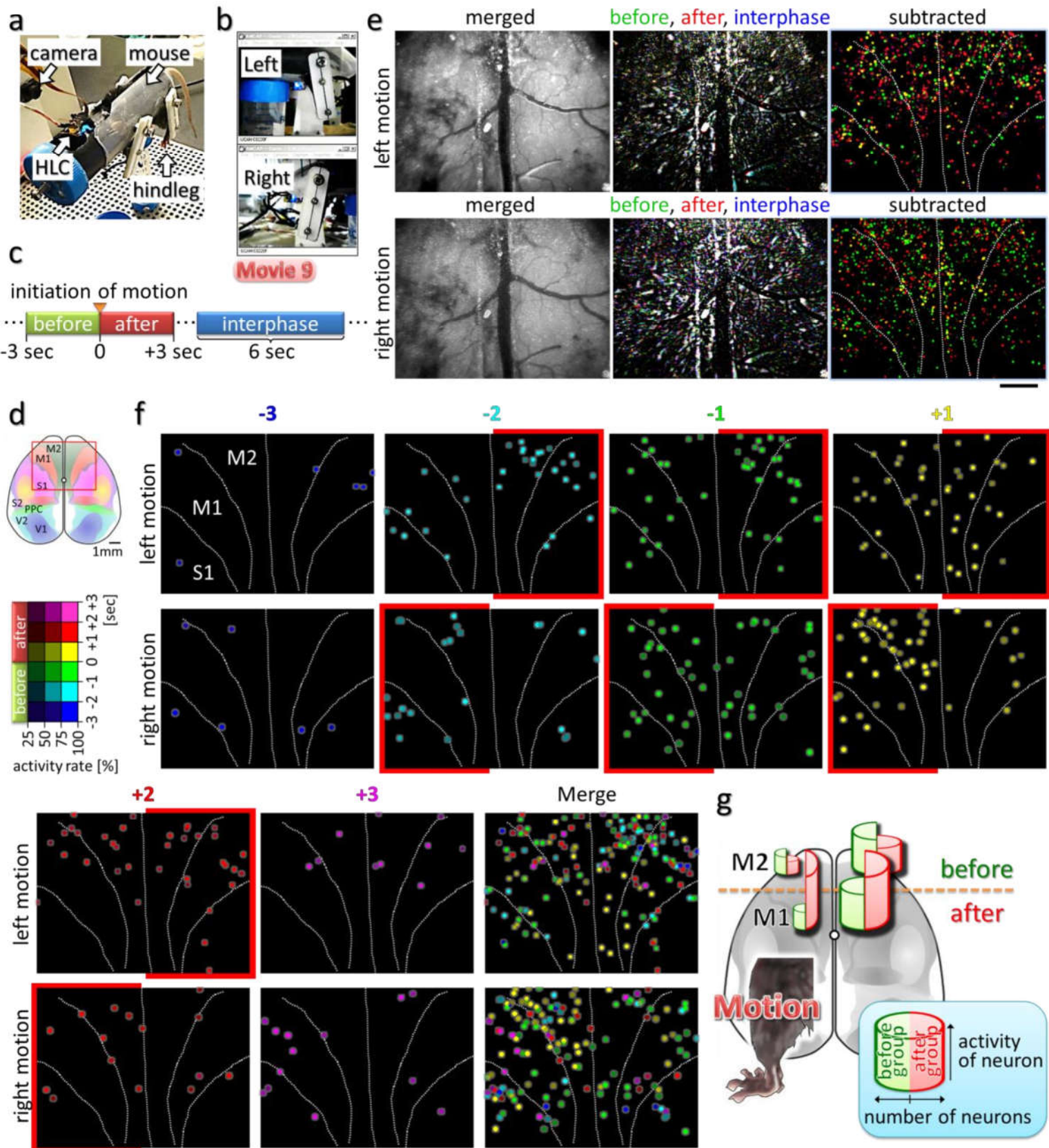
200 µm

f

baseline intensity

Fig. 7

Fig. 7
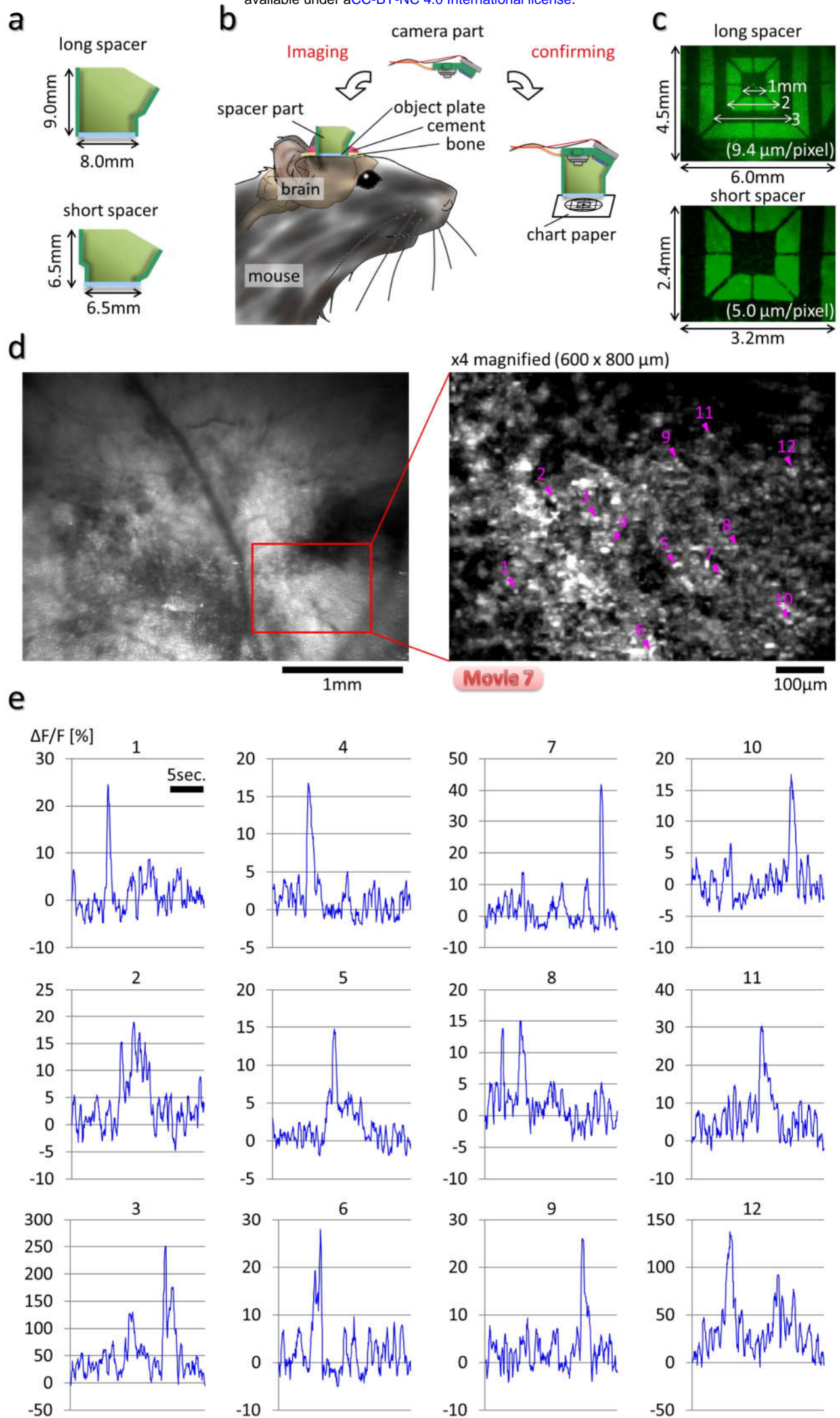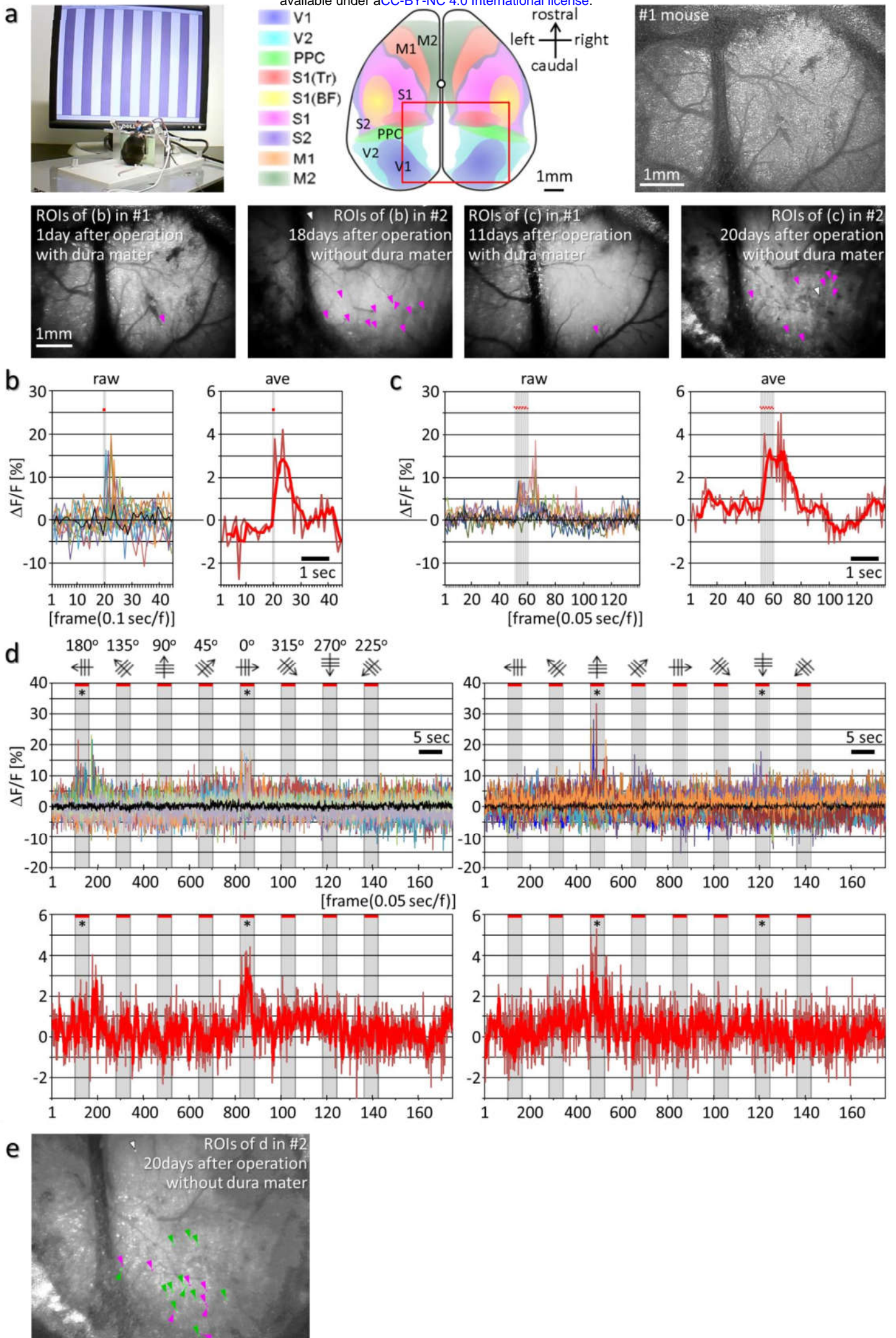
Fig. 8

Supplementary information

Wide and Deep Imaging of Neuronal Activities by a Wearable NeuroImager Reveals Premotor Activity in the Whole Motor Cortex

Takuma Kobayashi[1]*, Tanvir Islam[1], Masaaki Sato[2,3,4], Masamichi Ohkura[2,3], Junichi Nakai[2,3], Yasunori Hayashi[3,5,6], Hitoshi Okamoto[1]*

1. Laboratory for Neural Circuit Dynamics of Decision Making, RIKEN Center for Brain Science, Wako, Saitama 351-0198, Japan
2. Graduate School of Science and Engineering, Saitama University, Saitama, 338-8570, Japan
3. Brain and Body System Science Institute, Saitama University, Saitama, 338-8570, Japan
4. Laboratory for Mental Biology, RIKEN Center for Brain Science, Wako, Saitama 351-0198, Japan
5. RIKEN Center for Brain Science, Wako, Saitama 351-0198, Japan
6. Department of Pharmacology, Kyoto University Graduate School of Medicine, Kyoto 606-8501, Japan

*Corresponding author. Tel.: +81 48 467 9713; Fax.: +81 48 467 9714.
E-mail address: takuma.kobayashi@riken.jp; dr.takuma.kobayashi@gmail.com (T. Kobayashi), hitoshi.okamoto@riken.jp (H. Okamoto)

Supplementary Fig. 1
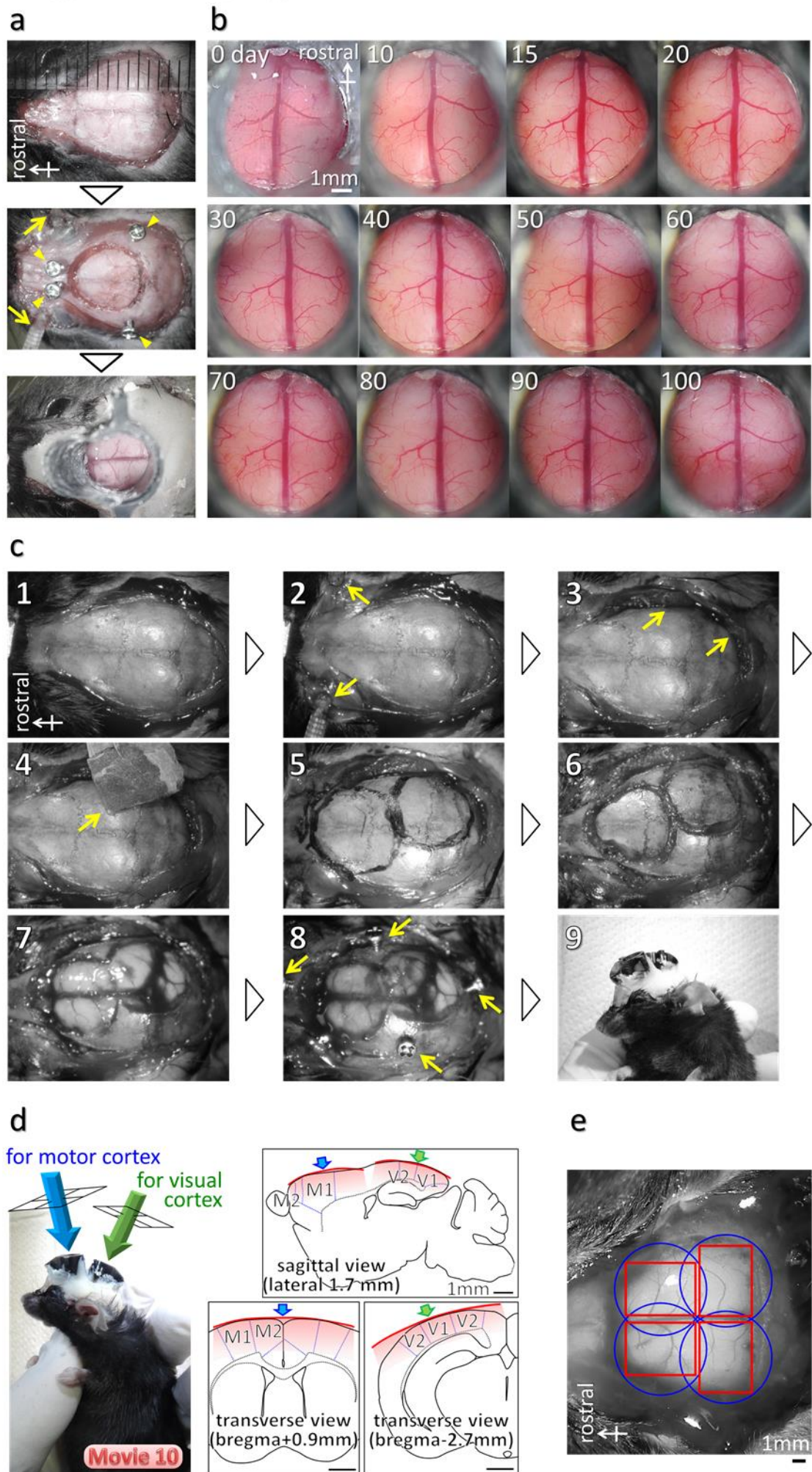
Supplementary Fig. 1 The HLC allows long-term observation of the same brain area in the same mouse.

(a) Typical surgical operation and the process of the applying a single use of the HLC. The mouse was anesthetized with 2,2,2-tribromoethanol (125-250 mg/kg body weight[40]) or a combination anesthetic consisting of 0.3 mg/kg medetomidine, 4.0 mg/kg midazolam and 5.0 mg/kg butorphanol[41], and was mounted on a stereotaxic instrument (Narishige Co., Japan). The head skin was scalped (upper panel). After craniotomy using a dental drill, the screws were inserted at bone positions around the hole to anchor the dental cement (yellow arrowheads in the middle panel). Eyelids were clamped with small forceps for protection (yellow arrows). The dura mater of the mouse was removed by using a hand-made sharpened tungsten needle gently and carefully. And then, the cylindrical spacer with a cranial window for imaging was attached to the mouse head by using dental cement (UNIFAST, GC, Co, Japan) (lower panel).

(b) Images show the temporal serial observation of the same mouse using a stereo microscope. Some part of the brain surface causes bleeding just after removing the dura although the extent of bleeding depends on operational skill. Bleeding was promptly stopped and the microvessels recovered in 4-5 days. Thereafter, the observation surface was kept clean for more than 100 days. During this long-term housing, neuronal activity could be visualized using the HLC and conventional 2-photon microscopy through the cranial window of the spacer apparatus (Supplementary Fig. 7).

(c) For multi-point imaging using two HLCs, surgical operation and the processes are shown. The detailed order of each process is described below;

1) Scalp removal.

2) Eyelid clamping using a small forceps for protection (yellow arrows).

3) Peeling part of the muscles of temporal and occipital regions (yellow arrows).

4) Removing the periosteum with water-resistant sandpaper (yellow arrow) (*e.g.* #600 waterproof paper file).

5) Marking the craniotomy position.

6) Drilling the skull by using a dental drill.

7) Removing the skull (optional: removing the dura mater).

8) Anchoring the screws (yellow arrows) (*e.g.* #0 pan head, M1.0 x 2.0 mm).

9) Attaching the cranial window parts with dental cement. Two cylindrical spacers with cranial windows were put on the cortex by using a precision manipulator to firmly support their positions, and then the spacers were fixed to the skull with dental cement. Besides, for behavioral testing under bright environments, black liquid rubber may be applied around the spacer and the dental cement for light interception.

(d) Example of installation of duplicate spacers for visual-motor imaging in the freely moving CaMK2a-G-CaMP7 mouse (Supplementary Movie 10). Blue or green arrows indicate the direction of observation from the HLC for imaging including the whole motor area of bilateral cortex or the

whole hemispheric visual area, respectively (left picture). The right panels show the directions of observation and the thick and convex area of imaging by the HLC (red line and graded red area, see also right image in Supplementary Fig. 6b) both in the sagittal (upper panel) and the cross (lower panels) sections. Use of multiple cameras allows the broad area imaging of the curved cortex at cellular resolution (>4.17 µm/pixel).

(e) Schematic image of the application of four HLCs. Blue circle and red square indicate the position of the spacer and the imaging area, respectively. The quadra imaging achieves simultaneous imaging of the entire cerebral cortex. As mentioned in Fig. 2a, one HLC can capture a wide field of view of 10.0 x 13.3 mm. This size is almost equal to one brain of the mouse. However, in that case, the resolution is lowered to 20.8 µm/pixel, and the sight from a single direction distorts the image of the spherical brain near its periphery. With multi-point thick imaging, it is possible to image at a high resolution with low distortion along the curvature of the cortex.

Supplementary Fig. 2
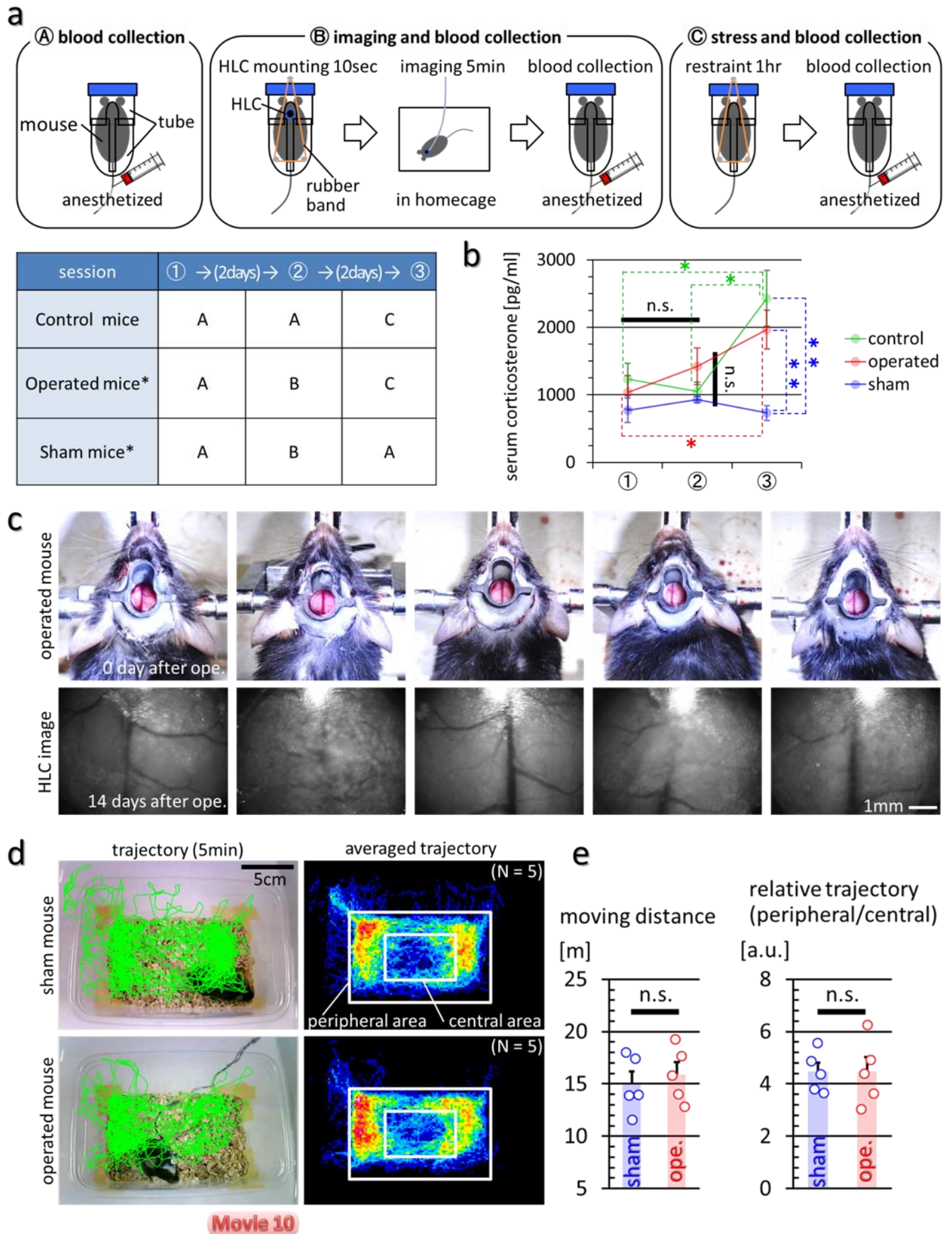
Supplementary Fig. 2 The imaging of neuronal activities by the HLC attached to the head of freely moving mice causes no significant increase of stress, and does not affect the locomotor activity and the behavioral pattern.

Blood-based and behavioral assessments of stress caused by wearing the HLC were performed.

(a) Corticosterone produced in response to stress was measured. Schematic images of experimental procedures are shown in A-C (upper images). These 3 different experiments were conducted in 3 sessions every 3 days for 3 groups of mice (each N = 5, total 15 mice) (lower table). 8-10 months old C57BL/6JJmsSlc male mice were purchased (Japan SLC, Inc., Japan). A group of mice with an asterisk were given the 5 minutes daily handling for 1 week prior to the experimental session. "Operated mice" were attached with the spacer apparatus with cranial window on his frontal cortical area by surgical operation performed 2 weeks before this experiment. "Sham mice" are the wild-type mice which underwent the same treatment as in the procedure B but were not mounted with the HLC.

(b) The result of ELISA assay of the serum corticosterone level is shown. All procedures were performed according to the manufacturer's protocol (Corticosterone ELISA Kit, Cayman Chemical Company, USA). Error bar is a standard error of the mean. T-test was performed after F-test for judging significance. Single asterisks mean there is the significance of $p < 0.05$ between session 1 and 3 ($p = 0.0271$), session 2 and 3 ($p = 0.0137$) in control mice, and between session 1 and 3 ($p = 0.0213$) in operated mice. Double asterisks mean there are significance of $p < 0.01$ between control and sham mice ($p = 0.0067$), operated and sham mice ($p = 0.0049$) in session 3. There are no significance (n.s.) between session 1 and 2 in all mice group, and between control, operated and sham mice in session 2. These results indicate that the HLC mounting and imaging process causes no significant increase in stress in the mice.

(c) These photos show the individual operated mice and their frontal cortical image taken by the HLC under the freely moving condition ("ope." means the surgical operation).

(d) The locomotor activity in the homecage from which the lid was removed was examined. Left column images indicate the examples of the moving trajectory for 5 minutes by a sham and an operated mouse (Supplementary Movie 10). Right column images indicate an averaged trajectory of 5 sham and operated mice. The averaged trajectories were binned with 5 x 5 pixels, and shown with pseudo-color. The bottom of the homecage was subdivided into the central and peripheral areas as indicated in the figures.

(e) The numerical analyses of (d) are shown in the graphs. Error bar is a standard error of the mean. Each circle indicates the value of each individual. There is no significance (n.s.) between the sham and operated mice in the moving distance or the distribution of the trajectory. These results suggest that HLC mounting and imaging process does not affect the locomotor activity and the behavioral pattern.
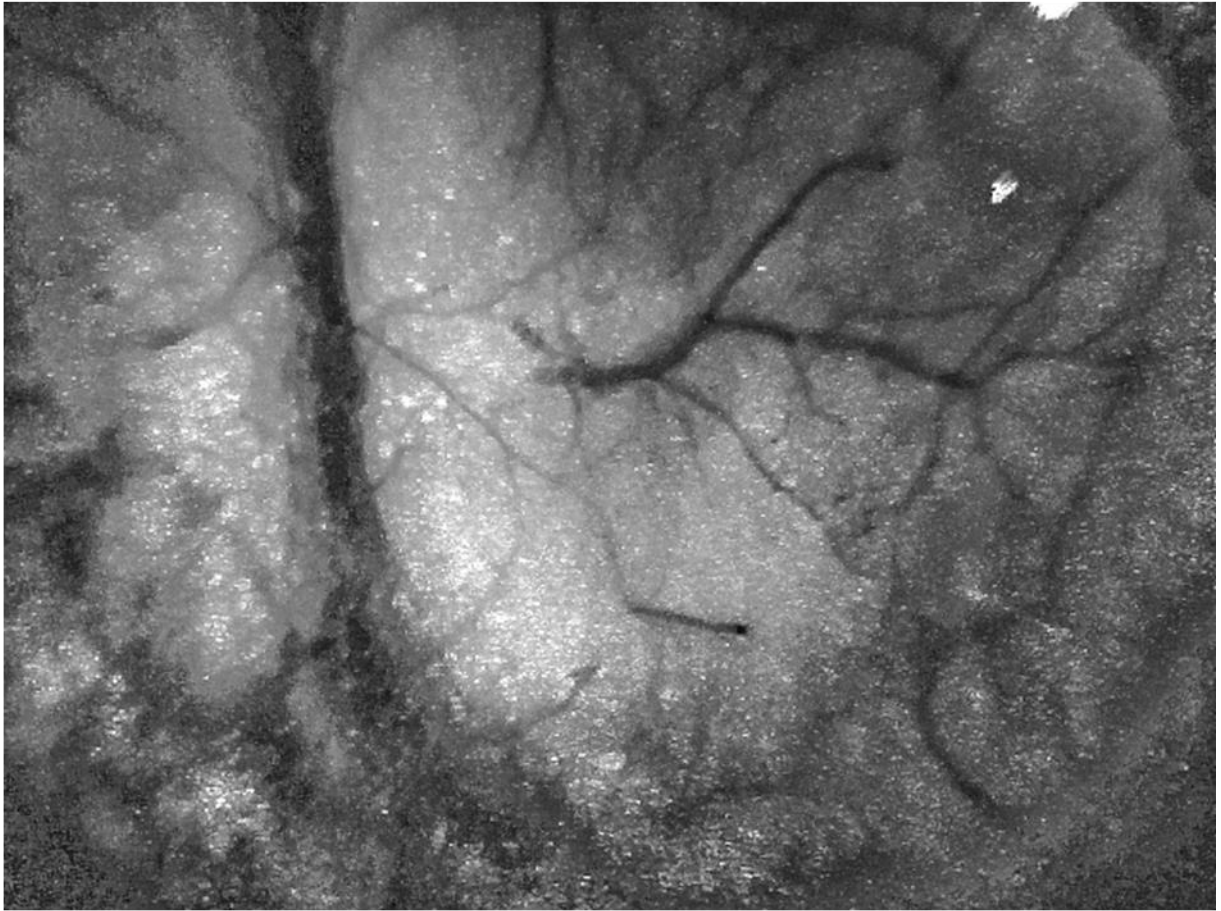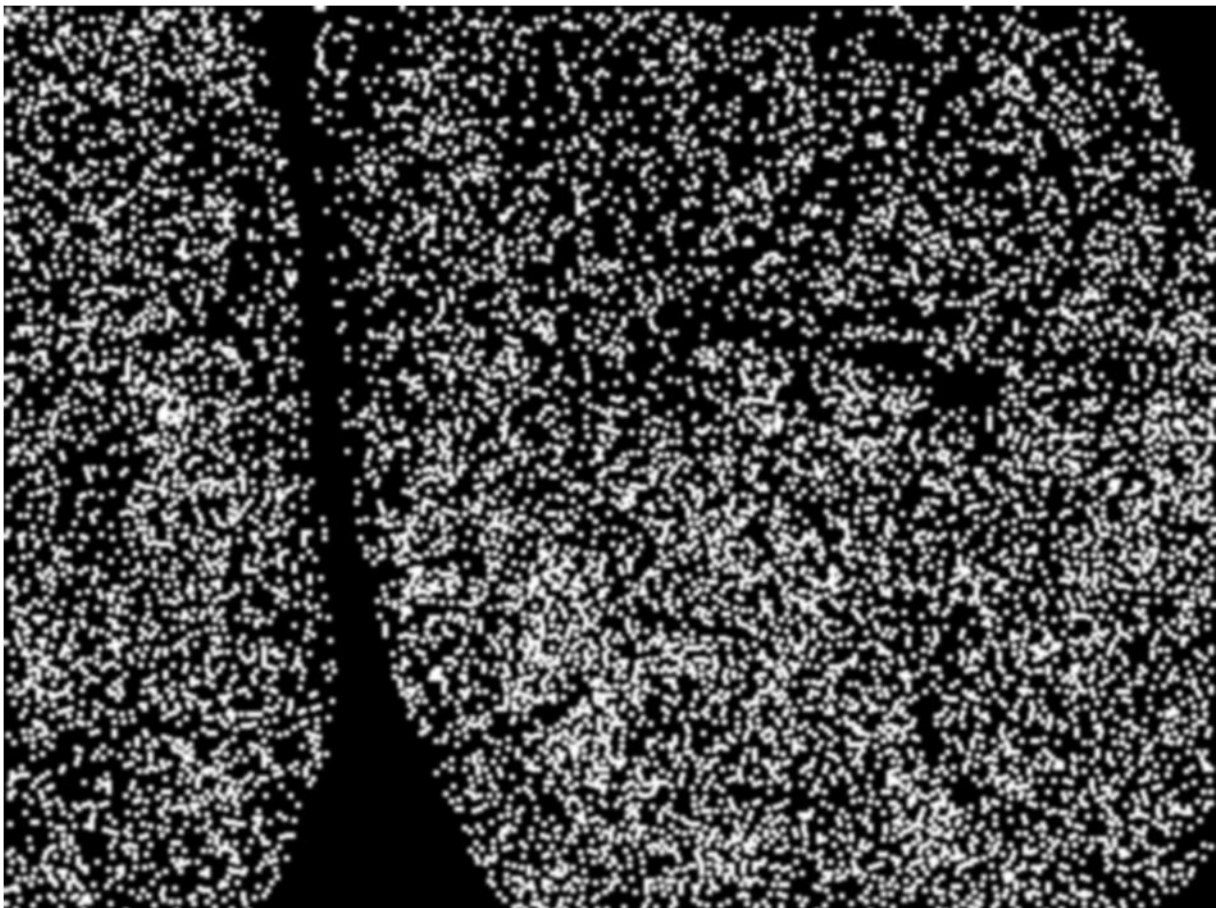
Supplementary Fig. 3

Supplementary Fig. 3   Automated selection and counting of discriminable blinking light spots.

(a, b) Ca^{2+} imaging was performed by the HLC on the visual cortex of the CaMK2a-G-CaMP7 transgenic mouse (Fig. 7). In order to estimate how many excitatory neurons can be detected and discriminated in the occipital area including the visual cortex by the HLC, the merged image was analyzed by counting the number of peak fluorescence spots (see for detail Methods section). 8 raw movies for 1 min were taken by the HLC and merged by maximization. A representative 10 seconds of the merged movie is shown in Supplementary Movie 3, and the results from where all frames were merged by maximization is shown in (a). Bar indicates 1 mm. The maximum points of the fluorescence spots of (b) are shown in (a). 9352 light spots could be discriminated within a single field of view by one HLC (4.25 x 5.66 mm, 30.7 x 10^4 pixels, 8.8 µm/pixel, 1-6 pixel/spot in (a), 5 pixel/dot in (b)).

Supplementary Fig. 4
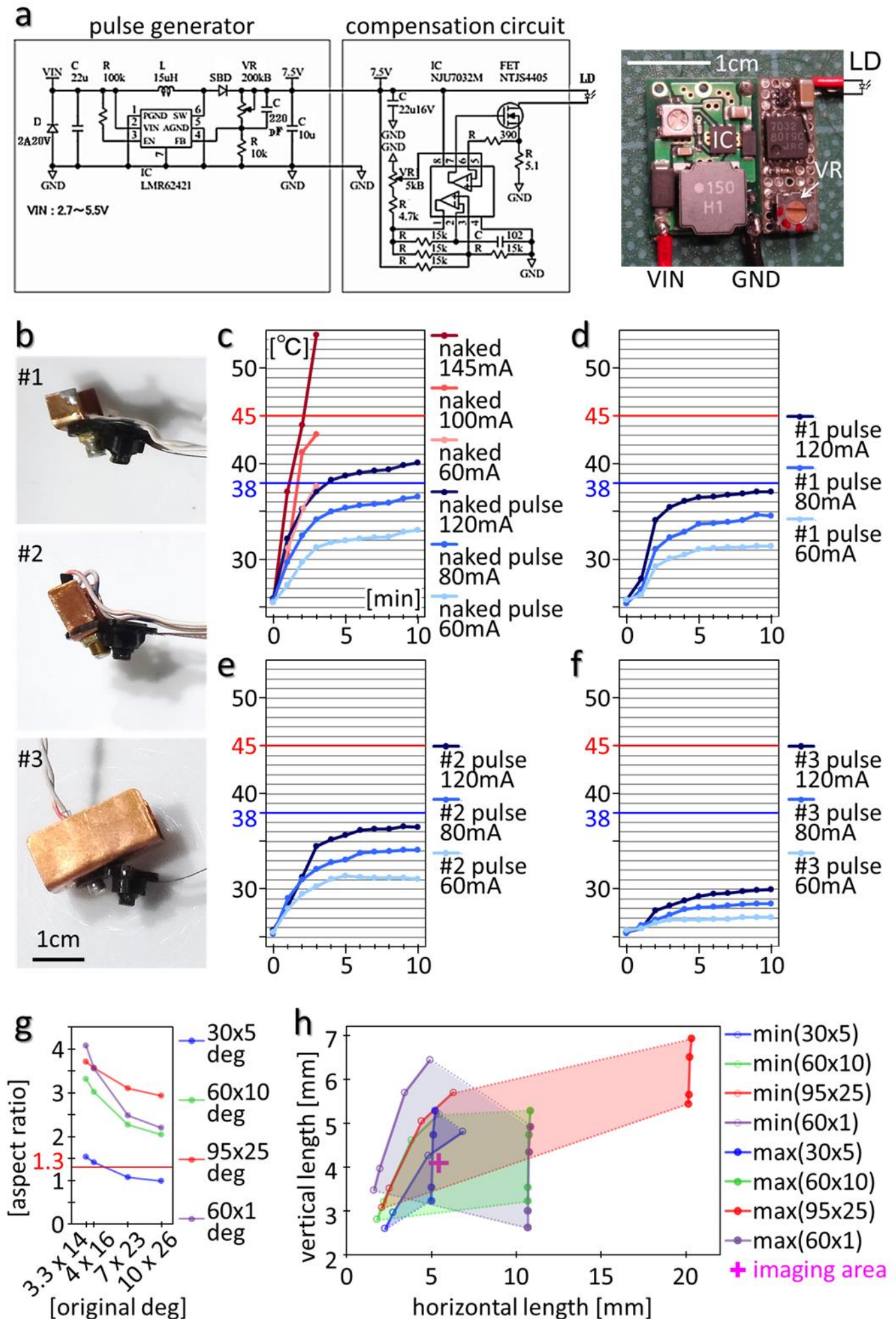
Supplementary Fig. 4 Components: a pulse generator to drive a laser diode (LD), an external heat sink structure to suppress the temperature rise of LD, and a light shaping diffuser (LSD).

(a) The LD driver and its circuit diagram. To prevent a temperature rise of the LD due to continuous illumination, a LD driver (ImageTech, Co., Japan) was regulated by a pulse generator which turns the LD on and off at a high-speed. In the circuit diagram, the left box shows an oscillator and the right box shows a compensation circuit. 32 kHz pulse is stably supplied to the LD. Since a source voltage allows 2.7-5.5 V input, the LD driver can be driven by an external power supply unit or also directly connected to the USB power supplying wire, which contributes to the miniaturization and simplification of the entire system. A CMOS operational amplifier was used in the compensation circuit for a constant current. MOS-FET (metal-oxide-semiconductor field-effect transistor) was used for an output enhancement as a switching element. Output power for LD can be controlled by a variable resister (potentiometer) (VR, white arrow in right image). Therefore, it is possible to irradiate excitation light with a preferable output according to the observation target during the imaging. VIN, input voltage; GND, ground; C, capacitor; R, resistor; L, inductor; D, diode.

(b) A heat sink of variable size was attached to the LD of the HLC. #1/ #2/ #3 shows 146.7/ 194.7/ 889.2 mm^2 heat sinks, respectively.
(c) The temperature change of the LD (PL450B, OSRAM, Inc., Germany, threshold current 30 mA, maximum optical output power 100 mW, threshold current 30 mA, operating current <145 mA) was examined. The temperature of the metal housing of the LD attached to the heat sinks was measured using a thermocoupled probe. The room temperature was 25.5 ^{o}C. Blue or red horizontal lines in each graph indicates 38 or 45 ^{o}C respectively, as a typical mouse's body temperature or as a presumptive limit temperature at which irreversible damage is caused to the cell. When a constant current of 60, 100, or 145 mA was applied to the "naked" LD (no heat sink), its temperature rapidly exceeded 38 ^{o}C (c). In contrast, when a pulsed constant current (32 kHz) of 60, 80, 120 mA was applied using a pulse generator, the temperature of the naked LD increased more slowly, finally reaching a plateau level after 10 minutes, thus showing the effectiveness of the pulse drive for stable lighting by the LD and the prevention of a rapid temperature rise.
(d-f) The temperature of the LD with the heat sink was measured. These results indicate that the cooling efficiency by the heat sink is higher as its surface area increases. The temperature of the LD with every type of heat sink reached a plateau without exceeding 38 ^{o}C, even if they were driven at 120 mA. Therefore, the heat sink structure is effective for cooling the LD. Also, the time of LD with the #1 heat sink temperature to reach 95 % of its maximum temperature was more than twice as fast as that of the naked LD. From a practical viewpoint, we decided to use the #1 sink in our *in vivo* experiments.

It is necessary to change the current value of laser diode (LD) according to the observation target. The experimenter needs to dim the LD while observing the fluorescence of the target during the experiment. As far as using the HLC (image sensor is OV7690) with the CaMK2a-G-CaMP7 mouse, it was mainly used at under 60-80 mA in most cases. At this situation, the temperature is

33.0 - 36.5 ^{o}C and it is below the body temperature of the mouse, so we do not need the heat sink (c). Since the LD is not in contact with the mouse and it is installed away from the mouse, even if it reaches 40 ^{o}C at 120 mA, it is considered that there is practically no problem if lighting is limited to short time. On the other hand, it is considered preferable to use a heat sink if it is expected to be used for longer period at approximately 90 mA or more. In this condition, LD is expected to exceed the mouse body temperature (depending on the room temperature).

The heat sink suppresses the temperature rise above the room temperature, and shortens the time to reach the plateau, so it stabilizes the laser light quickly. Therefore, the experimenter can shorten the standby time associated with turning on and off the LD. In summary, if the experimenter emphasizes weight reduction of the HLC, it is not necessary to attach the heat sink. While, if the experimenter wishes to give priority to shortening the standby time, it is effective to attach the heat sink.

(g, h) The LD is used as the excitation light source of the HLC. The laser light from LD has a flat shape (lower leftmost panel in Fig. 2h). Therefore, the irradiation beam was processed by using a light shaping diffuser (LSD). In the right panel of Fig. 2g, the LD was tilted 30 degrees from the light axis of the camera and the paper was illuminated from a distance of 8 mm, which is the same condition as actually used in the HLC. As a control, we used a white LED that projected a round light bundle. The projected images by the white LED with a circle lens or LD (PLT5 488, OSRAM, Inc., Germany) were taken in the dark by a digital camera (COOLPIX P7100, Nikkon, Inc., Japan) with ISO100, exposure time 1 second, and fixed focus. The oscillation threshold of the LD, PLT5 488, is 30 mA, and the maximum limit current is 150 mA. According to the specification, the original beam divergence changes in the range of 4 x 16 - 7 x 23 (at 75 mA) - 10 x 26 degrees (deg) depending on the amount of applied current. Since the LD is usually driven at 40-80 mA for *in vivo* imaging, the distribution of LD at 40 mA was first analyzed. In the upper line of Fig. 2h, the projected circle light by the white LED was processed to a horizontal ellipse shape with various LSDs; original, 30 x 5 deg, 60 x 10 deg, 95 x 25 deg, 60 x 1 deg. Similarly, the figures in the lower line show that the projected vertical elliptical light from LD was processed to horizontal ellipse shape. In the result of the light projection using the 60 x 10 deg LSD, the distribution of a yellow-colored area with a half-value intensity was within an inner red square which corresponds to the typical view field of the HLC (4.0 x 5.3 mm). Therefore, we thought that the light distribution processed by the 60 x 10 deg LSD most closely matches the region of the imaging field of the HLC.

Continuously, the aspect ratios of the diffusion angle of the projected beam by the various LSDs were calculated depending on the original divergences of the LD at different currents (g). And finally, the various projected ranges by the various diffusion angles were simulated (h).

The graph in (g) indicates the aspect ratio of the vertical and horizontal projected angle in each diffusion angle LSD (indicated by different colored lines) plotted against various divergences of the original LD beam at different currents. X-axis values are plotted according to the horizontal degree of the original LD beam. The aspect ratio of the imaging area of the CMOS, *i.e.* 640 x 480 pixels, is 1.33 (led line).

When the LSD is applied, the diffusion angle is approximated by the following formula: $\sqrt{}$[(light source divergence angle)^2 + (LSD diffusion angle)^2], and the diffusion range is approximated by the following formula : (the distance to irradiated surface) x 2 tanθ, where θ is the half of the diffusion angle. In this experiment, the light source position was tilted by 30 deg horizontally. Therefore, the distance to the irradiated surface was 8 mm x $2/\sqrt{3}$, and the horizontal diffusion range was also corrected by multiplying $2/\sqrt{3}$. From the measurement result based on the projected original image in Fig. 2h, the original beam divergence of LD was 3.3 x 14 deg at 40 mA. In the case of 3.3 x 14 deg, the shape tendency calculated by the corrected angle at various aspect ratios of the LSD coincides with the actual distribution in Fig. 2h.

As a result, a 30 x 5 deg LSD is the most preferable and 60 x 10 deg LSD is the secondarily preferable for all current ranges of the LD.

The graph in (h) indicates the various projected ranges (vertical, horizontal length) by the various diffusion angles of the LSD (indicated by different colored lines) at the minimum or maximum current of LD. The diffusion angle increases or decreases according to an increase or decrease of the current value. The minimum projected ranges with various LSDs by the minimum current were calculated based on the yellow-colored area of projected image of Fig. 2h, and are shown as "min (LSD variation)" on the right side of the graph. Similarly, the maximum projected ranges were estimated based on 3.3 x 14, 4 x 16, 7 x 23, 10 x 26 deg as a maximum original divergence, and are shown as "max (LSD variation)". The four dots in the data for each LSD show the results in order of the current value. The colored area for each type of LSD indicates the projected range that can change from the min value to the max value. "Imaging area" (magenta cross in the graph) indicates the typical HLC imaging area (4.0 x 5.3 mm). As a result, all tested LSDs except the 30 x 5 deg LSD can cover the imaging area.

From these results, the 60 x 10 deg LSD is the most preferable for the LD of the HLC under the various assumed usage conditions.

Supplementary Fig. 5
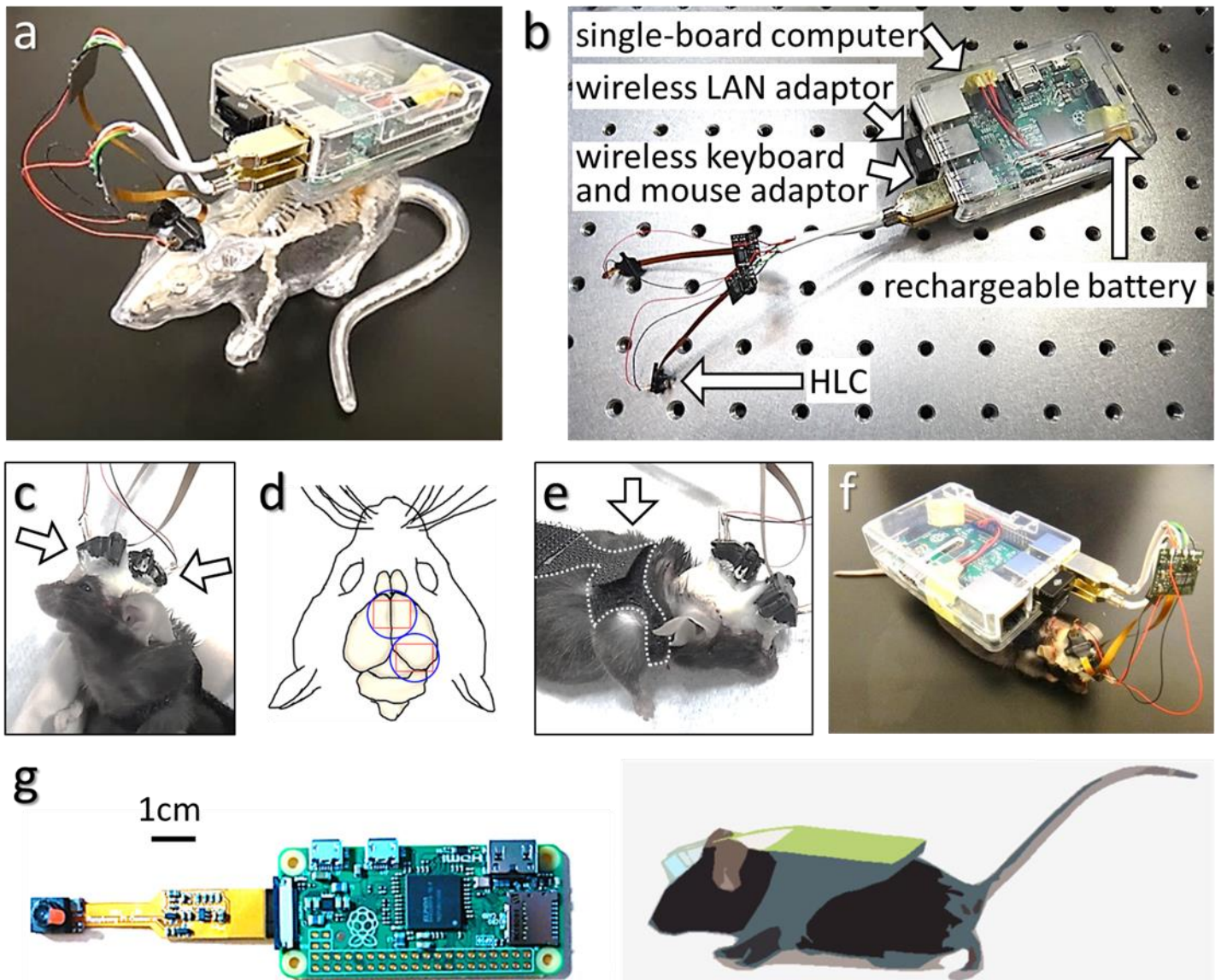
Supplementary Fig. 5 Wearable on-demand wireless imaging system using single-board computers.

An on-demand device is preferable for real-time observation of natural behaviors. Therefore, we constructed several types of wearable wireless units by using single-board computers. The CMOS image sensor used in the HLC is more compact and can work on lower power than a CCD (charge-coupled device), and is suitable for wireless control.

(a, b) Examples of a wearable on-demand wireless imaging system are shown. Dual HLCs were applied to the visual cortex of both hemicephalons on the rodent maquette (a). A Raspberry Pi 2 model B (Raspberry Pi Foundation, UK) was used as a main single-board computer (b). This multi imaging system is composed of the HLCs and adaptors for wireless LAN, keyboard, and mouse. Therefore, it can autonomously perform imaging and recording, and accept control from other PCs as a slave and send real-time video by remote operation. The wireless multi imaging system whose weight is 48 g can run for approximately 6–10 minutes with a rechargeable battery. The operating time can be extended depending on battery capacity.

(c) An example of multiple uses of the HLC is shown (see for detail Supplementary Fig. 1c, d).

(d) A schematic image of the applied position of (c) where the frontal or occipital cortical area including the motor or visual cortex is shown. The blue circle and red square indicate the spacer position and the imaging area, respectively.

(e) The image indicates the mouse wearing a vest to attach the device. In order for the mouse to move freely, it is necessary to carry the unit on its back (see also schematic image in (g)).

(f) An example of the wireless multiple imaging system (a) applied to a C57BL/6 line mouse. However, the weight and size of this type of system are slightly large and heavy for the tiny body of mouse. For instance, the ICR mice line that has a relatively large body size, a rat, or other large animals will be suitable for this wireless system.

(g) The system can be scaled down by using Raspberry Pi Zero as shown. Raspberry Pi Zero is smaller and lighter than Pi 2, approximately 1/12 by volume. Therefore, this type of wearable wireless imaging system will be more suitable for small animals such as the C57BL/6 line mouse.

Supplementary Fig. 6
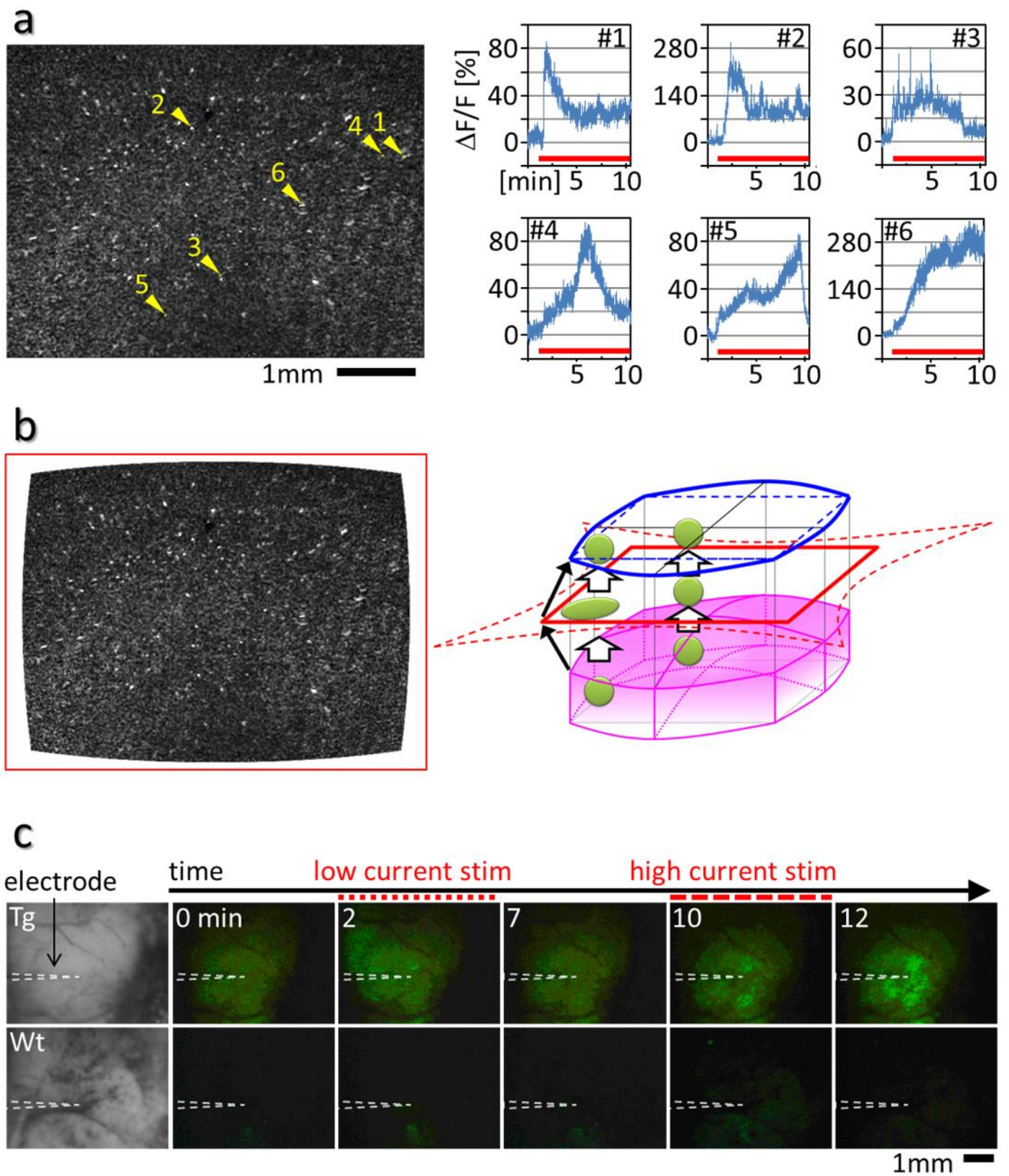
Supplementary Fig. 6   The HLC can visualize intracellular Ca^{2+} dynamics of individual cells in 3D culture and artificially evoked neuronal activities by electrostimulation in the deep cerebral layer.

(a) The results of individual analysis of the Ca^{2+} imaging by the HLC of the 3D cultured Hela cells that were transfected with the G-CaMP6 gene (Fig. 4a) are shown. The 106 fluorescence spots in the imaging movie (10 frame/sec, 10 min) were selected randomly as a 1 or 4 pixels ROI. The mean of fluorescence intensity (FI) changes at each ROI and the change rate of FI ($\Delta F/F$) was calculated as $(F-F_0)/F$, where F_0 is the mean FI of the first 10 frames in each ROI. The maximum $\Delta F/F$ was 693.3 % in these ROIs. The positions of a representative 6 ROIs are shown by the arrowheads with numbers in the image of (a), and their $\Delta F/F$ are shown in the graphs and movie (Supplementary Movie 4). The fluorescence intensity was increased after histamine administration (red line in the graph). The graphs are arranged in chronological order of the timing of the $\Delta F/F$ peak appearance. The results indicate that the fluorescence functional cell imaging that represent the Ca^{2+} dynamics within each cell can be performed by the HLC at single-cell resolution.

For traditional 2D culture conditions without embedding into the extracellular matrix gel, the FI of the Ca^{2+} indicators usually promptly starts to increase just after histamine administration, or within 2 minutes at the latest (supplemental information in the previous study[12]). Under the 3D culture condition, however, the response may be delayed for longer periods depending on individual cells, sometimes as long as more than 10 minutes. Such a delayed response might depend on the depth of each cell because there should be a natural time lag in the diffusion of the histamine into the interior of the gel.

(b) The left image of (a) was corrected with DTV (television distortion) -3.9 % according to the result of Fig. 2a. Red square line indicates the image silhouette of (a). The right schematic diagram shows the correction process of the image. Magenta block indicates the thick convex image area of the HLC. The magenta gradient schematically represents the difference in fluorescence detection ability according to the result of Fig. 3e. A red line indicates the image silhouette of (a) that is taken by the HLC. The red broken line indicates the positive pincushion distorted actual image of the original object (magenta block). The blue line indicates the negative barrel compensated image of the red line, and also indicates the restored original image silhouette of the object (magenta block). The blue broken line indicates the predicted non-compensated image of the blue line, in other words, the positive barrel distorted image of the blue line. The distortions of the schematic images are enhanced for the ease of visual understanding. Black arrows show the same corner of each image. Green circles indicate the cells. The distortion is smaller near the center of the original object, while the distortion is larger near the edge of the original object. Therefore, the cell shape that was enlarged at the periphery in the image taken by the HLC is corrected to the original size in the restored image (left picture).

(c) Ca^{2+} imaging was performed by the HLC on the somatosensory cortex of the Thy1-G-CaMP7 transgenic mouse (Fig. 4c, d). We performed Ca^{2+} imaging with the HLC for evoked activity before

Ca^{2+} imaging of other physiological neuronal activities. In this experiment, an HLC equipped with 450-460 nm LD, 30 x 5 deg LSD and >520 nm emission filter was used. After craniotomy, a coaxial electrode (TOG207-078, Unique Medical Co., Ltd., Japan) was inserted into the somatosensory cortical layer 5/6 at around 500-600 μm depth using a micromanipulator. Then, a low or high tetanic stimulation (3 or 10 mA biphasic square waves, 100 Hz, duration 150 μs, interval 10 ms, 3 sec.) was applied by using a stimulator (Isolated pulse stimulator 2100, A-M Systems Inc., USA). The time lapse imaging data of the *in vivo* experiment (Fig. 4c, d) on the Thy1-G-CaMP7 mouse (Tg) or wild type mouse (wt) for the negative control are shown. The electrode was inserted into the cortex from the side after the craniotomy. The HLC was attached on the cortex and then the Ca^{2+} imaging was performed. When the stimulation was applied, the FI increased around the electrode in the Tg mouse, and the response was greater after high current than low current stimulation. In contrast, similar evoked signals were not detected in a wt mouse. These results indicate that the HLC can detect evoked neuronal activities in the cortex. Especially, it is thought that these changes of the FI mainly reflect the activities of the layer 5/6 pyramidal neurons and its neurites, because the Thy1 promoter is activated in those neurons predominantly.

In the wild-type case, slow and slight increases of the FI were also detected after stimulation. It is thought that this reaction reflects the intrinsic flavoprotein fluorescence in mitochondria[41]. The excitation peak is near 450 nm, therefore, the endogenous flavoprotein imaging depending on neural activity is also accessed by the HLC although the amount of FI change is much smaller, and the response speed is much slower than G-CaMP. Such flavin imaging would allow the functional neuronal imaging in the completely intact brain.

Supplementary Fig. 7
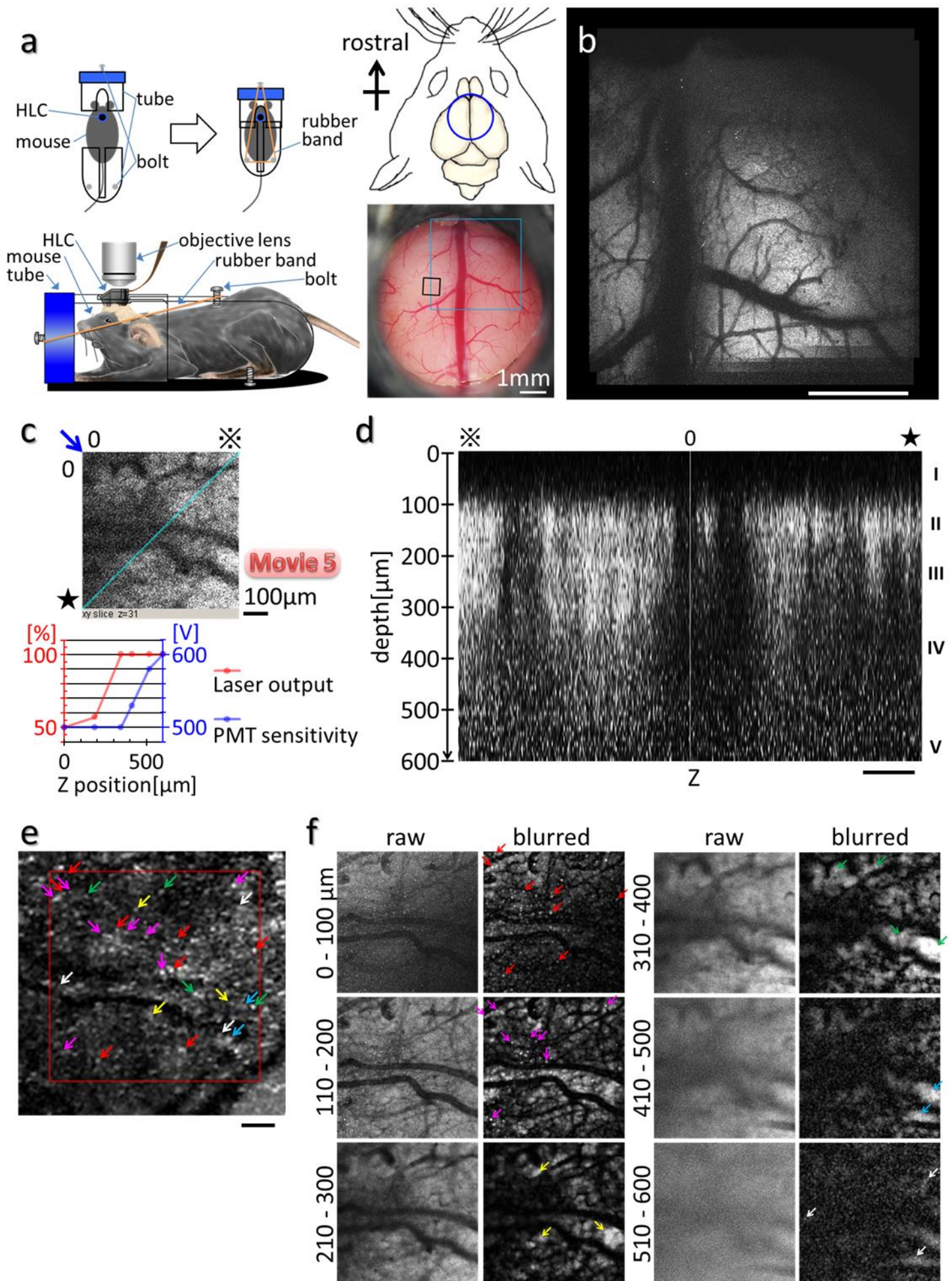
Supplementary Fig. 7 The spacer apparatus with the cranial window allows the HLC and 2-photon microscope to perform chronic Ca^{2+} imaging at the same position in the same mouse.

(a) Fixation of the mouse head with the HLC on the head. After craniotomy and removal of the dura mater, the CaMK2a-G-CaMP7 mouse (mouse ID: # 3) was installed with the spacer apparatus with a cranial window on the frontal cortical region (see for detail Supplementary Fig. 1a, b). Then, fluorescence imaging was performed by using a 2-photon microscope (FVMPE-RS, Olympus, Co., Japan) at 5-6 days (b) and 33 days (c, d, f) after the surgical operation. The mouse was held in a plastic tube with the head fixed by the attachment of the HLC spacer to the hole of the tube (schematic image of left panel). The schematic image of the right upper panel indicates the location of the cranial window (blue circle). The right lower image was taken by a stereo microscope through the cranial window. Blue or black square indicates the imaging area of (b) or (c, d, f), respectively.

(b) The fluorescence imaging was performed in the awake condition with a 2-photon microscope using a galvano scanner. The view field was 3.18 x 3.18 mm, 512 x 512 pixels, 6.21 μm/pixel, and images were captured 10 times at 1.01 sec/stack at the depth of 300 μm. The acquired imaging data were merged. Misalignment caused by mouse movements between stacks was corrected manually, and a "maximum intensity projection", *i.e.* a creation of the image where each pixel contains the maximum value over all images in the stacks, was performed. The result is shown in (b). Each fluorescent spot should represent excitatory neurons. Bar indicates 1 mm.

(c) The fluorescence imaging was performed with a 2-photon microscope using the galvano scanner in the anesthetized condition (upper panel). The view field is 636 x 636 μm, 512 x 512 pixels, and the images at 0.917 sec/stack were captured to a depth of 600 μm every 10 μm. The image shows a horizontal section of the cerebral cortex at the 31th stack, that is, a depth of 300 μm. The blue line and blue arrow indicate the position of the vertical section of the cortex and the direction of view in (d). The reference marks of two type asterisks correspond to the positions shown in (d). The lower graph indicates the imaging setting. Depending on the depth, the laser output and PMT (photomultiplier tube) sensitivity of the 2-photon microscope were changed.

Time-lapse imaging of the same view area in (c) at a 120 μm depth of the anesthetized mouse cortex was performed with a 2-photon microscope using a resonant scanner. The 10 times speed movie that was captured at 389.72 ms/frame and averaged at every 10 frames is shown in Supplementary Movie 5. Since the resonant scanner allows faster capture than the galvano scanner, the blinking of fluorescence spots is easier to recognize. It is thought that those fluorescence spots blinking represent the activity of excitatory neurons.

(d) Image shows the vertical cross section of the cortex (c). The length of 0-※ and 0-★ are 900 μm. Roman numerals on the right side of figure indicate the layer of the cortex. Bar indicates 100 μm.

(e, f) The fluorescence image of the same mouse as (a) which was taken by the HLC under the freely-moving condition at 57 days after surgical operation is shown in (e). Red square shows the imaging area by 2-photon microscopy, which is the same as the black square in (a). Bar indicates 100 μm. Each colored arrow roughly corresponds in position to the light spots in (f). The image of

(e) is the result of the processing as the following. The fluorescence movie data taken by the HLC for 5 minutes at 50 ms/frame (20 fps) was deconvoluted and background subtracted, and all frames were merged to one image by a maximum intensity projection.

In (f), the fluorescence images of the anesthetized mouse were taken by 2-photon microscopy. Bar indicates 100 μm. The images at 1.00 sec/stack were captured to a depth of 600 μm at every 10 μm intervals (see for the Z axis reconstruction data in (d)). And then, images were superimposed every 100 μm by the maximum intensity projection of each of 10 slices, as shown "raw". The blurring with a radius of 3.8 pixels at the light spot of that raw imaging data was performed as shown "blurred" by using a Gaussian filter of ImageJ. We performed this blurring procedure to match the resolution (9.62 μm/pixel) by the HLC whose view field in this experiment is 4.62 x 6.16 mm, 480 x 640 pixels to the resolution (1.24 μm/pixel) by 2-photon microscope. The difference in resolution between the HLC and 2-photon microscope is 7.7 times, therefore the radius of 3.8 pixels blurring was performed to obtain similar images.

As a result, during the long-term housing, neuronal activity could be visualized using the HLC and also by conventional 2-photon microscopy through the cranial window of the spacer apparatus.

Supplementary Fig. 8
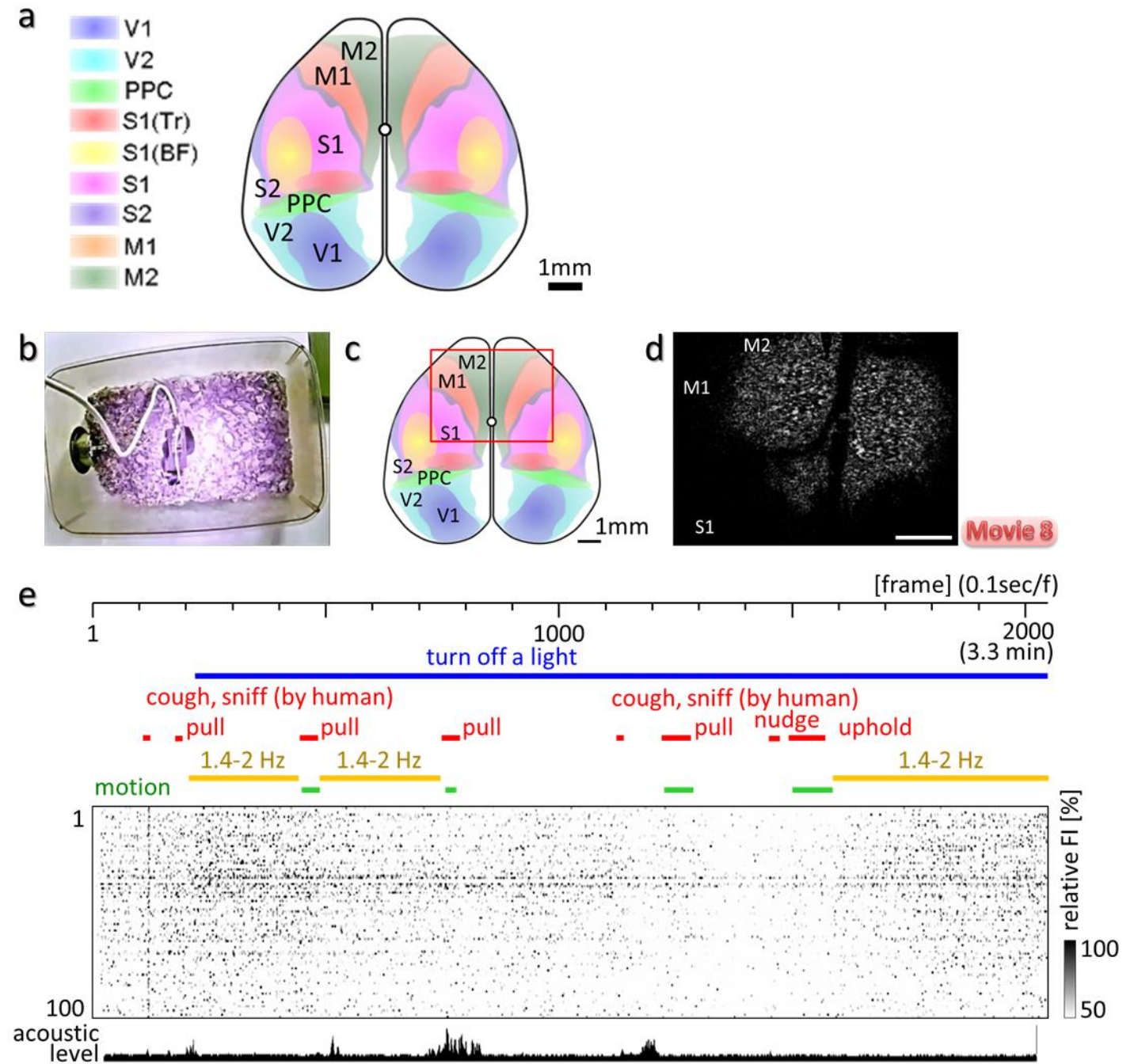
Supplementary Fig. 8   Event related neuronal activity was observed in the frontal cortex in the freely moving condition

Ca^{2+} imaging was performed with the HLC in the freely moving CaMK2a-G-CaMP7 mouse in the square cage. The behavior of the mouse was taken with an IR web camera placed above the cage.

(a) The schematic image shows the cerebral cortical map which was partially modified from the map[37] reconstructed from the serial coronal sections of the brain atlas[36]. Each abbreviation means V1/2, primary/secondary visual cortex; PPC (PtA), posterior parietal cortex (parietal association cortex); S1 (Tr/BF)/S2, primary (trunk/olfactory barrel field)/secondary somatosensory cortex; M1/2, primary/secondary motor cortex.

(b) The image shows the experimental setup.

**(c)** The schematic image of the HLC imaging area is shown (red square).

(d) The subtracted fluorescence image of the frontal cortex (c) in the CaMK2a-G-CaMP7 mouse taken by HLC under the freely moving condition (b) is shown. The raw movie (10 frame/sec) was subtracted by the averaged frame of the first 10 frames of the movie, and then the brightness and contrast was enhanced to observe neuronal activity in association with behavior as shown in (d, Supplementary Movie 8). Bar indicates 1 mm.

(e) 100 fluorescent spots of 4 pixels were picked up at random as representative ROIs from both hemispheres broadly based on the raw data. A temporal change of the FI in each ROI is shown by the raster plot. Several interventions were applied to the mouse during Ca^{2+} imaging (notation in red). The bottom graph shows an ambient acoustic level. The spacer of the HLC was shielded from light by the additional liquid rubber coat, and the changes in the surrounding lighting had no direct influence on the imaging result. The blue line indicates the period of dark environment, and the mouse behavior could still be observed by the IR web camera. Since the HLC has an IR cut filter (<650 nm), IR lighting also had no direct influence on the imaging result. The green lines indicate mouse motion.

When pulling, nudging, and upholding the mouse body were repeatedly conducted during Ca^{2+} imaging of the frontal cortex, neuronal activity changed in relation to these events. When the experimenter coughed near the mouse, transient and overall activity occurred in many ROIs. However, such a global reaction was not caused by a second cough, possibly due to acclimation. Broad slow synchronized wavelike activity propagated sometimes at the resting state during the periods indicated by yellow lines. Such a slow wave response was interrupted by a pull, and does not always occur during the resting period, which suggests that the phenomenon is not just noise. This slow oscillatory activity may be similar to the one observed during the inter trial periods[43].

Supplementary Fig. 9
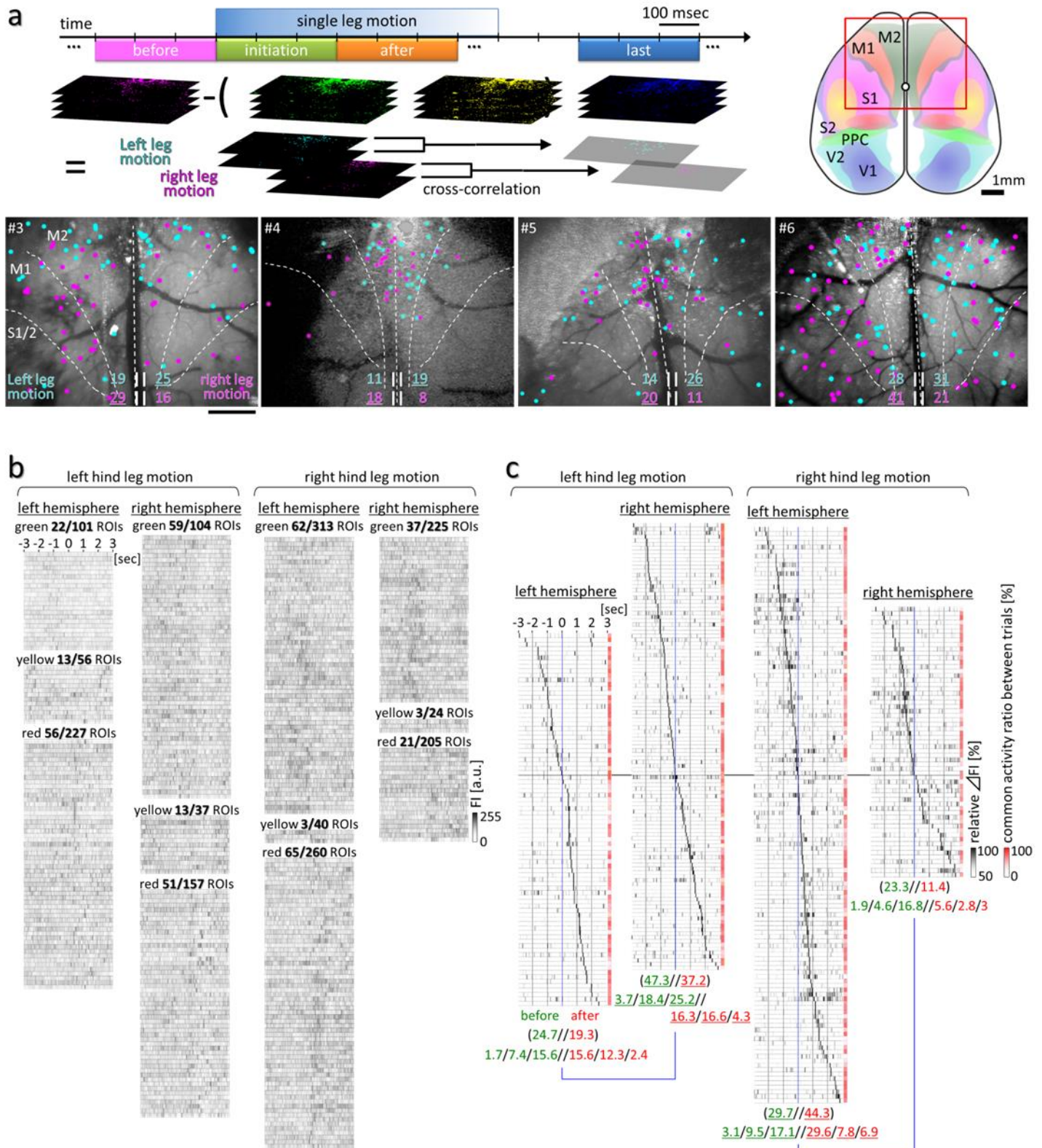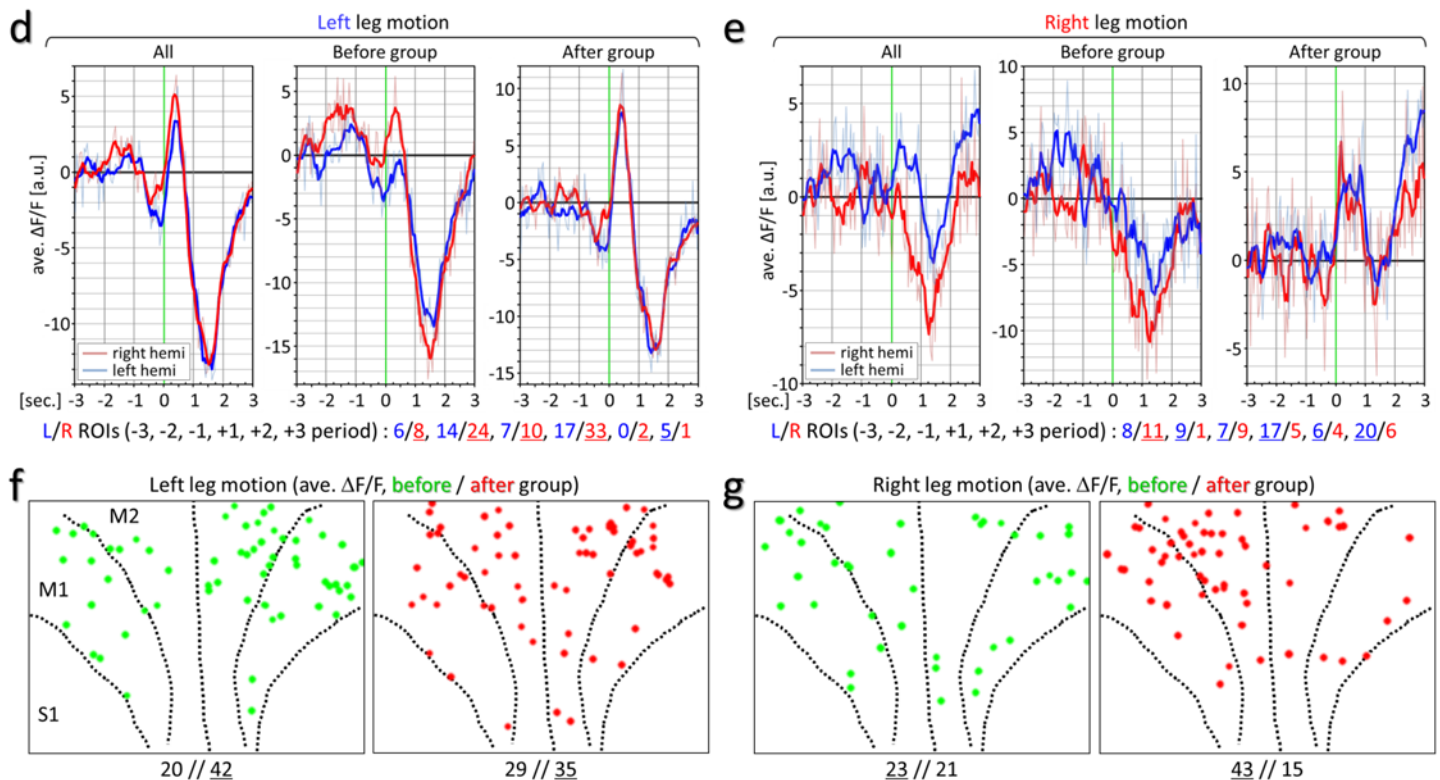
Supplementary Fig. 9 Cross-correlation analysis and the relative ΔFI in the comprehensive quantitative analysis reveal the specific cell assemblies which represent a cascadic premotor activity during voluntary movement.

(a) The result shows the cross-correlation analysis of premotor activity. In the CaMK2a-G-CaMP7 mouse, 10 or 20 fps (frame per second) Ca^{2+} imaging was performed over the frontal cortex including the whole motor cortex by the restriction motion experiment and the HLC (Fig. 8a). The left schematic image indicates the process of the analysis method. The middle schematic image shows the imaging position by the HLC. The red square indicates the imaging area by the HLC, 5.0 x 6.5 mm. The activity positions of excitatory neurons during the 300 ms before the onset of the left or right hindleg motion were extracted in the process as described below. First, 4 periods for 300 ms during the left or right hindleg's voluntary movement were categorized as "before", "initiation", "after" and "last". For example, "before" or "initiation" was defined the period just before or after the onset of the motion, respectively. "After" was defined as the period just after "initiation". "Last" was defined as the period from 200 ms just after the motion stopping. Next, fluorescence imaging data from each of the 4 periods was subtracted by the data of the one frame just before each period to reduce the background. Those subtracted imaging movie data were converted to a one frame image by maximization, and then, the subtraction between each period, max of "before" – max of ["initiation" + "after" + "last"], was performed for each ROI. The result was expected to represent only premotor activity. Finally, the image of two discrete trials accompanying the left or right

hindleg's motion in the same mouse are shown for comparison in the lower images of (a). The results of 4 mice are shown (mouse ID: #1 - #4). Bar indicates 1 mm. Cyan or magenta dots indicate the neurons activated before the left or right hindleg motion. For example in #1 mouse, 19 and 25 neurons of the left and right hemisphere, respectively, were activated before the left leg motion. And 29 and 16 neurons of the left and right hemisphere, respectively, were activated before the right leg motion. These neurons seem to be more localized to M2 than M1, and are rarely present in the other areas such as the somatosensory cortex, and its localization is biased toward the contralateral side over the motion side.

The results of (b, c) show a part of the comprehensive quantitative analysis of the premotor activity in Fig. 8.

(b) The temporal value changes of FI, derived from the raw 20 fps Ca^{2+} imaging data, at ROIs in the subtracted image of Fig. 8e with >5 % $\Delta F/F$ are presented by a raster plot. The numbers at the top of each raster plot mean [>5 % $\Delta F/F$ ROIs] / [all ROIs]. The ROIs were classified by color codes (green, yellow and red) according to the criteria described in the legend of Fig. 8e. The yellow ROIs are double positive for both green and red characters.

(c) The data shows the temporal raster plot of relative FI change rates of (b) (relative ΔFI [%]), and an averaged possibility of all kick events at each ROI (red boxes). The relative ΔFI was calculated so that a minimum or maximum value was set to 0 or 100 for each ROI in data of (b). Then, the 50-100 % relative ΔFI in each ROI was presented by the order of the peak point time. The possibility value was calculated based on whether the subtracted FI at each ROI in each kick event was positive (= 1) or negative (= 0). The averaged possibility values at each ROI in all kick events are indicated by red boxes at the right end of the raster plot line. The sum of possible values is indicated by the number under each raster plot. Green or red colored numbers mean the sum before or after the initiation of the motion. The bottom numbers mean the sums within each time period (-3 to -2 / -2 to -1 / -1 to 0 // 0 to 1 / 1 to 2 / 2 to 3 [sec]). Underline means the larger numbers compared to those on the other side of the hemisphere. These results also indicate the tendency that many active ROIs exist in the contralateral hemispheres from the motion side similar to the result in (a).

Next, an overall qualitative analysis was performed to eliminate the concern that accidentally large but rare activities might make unduly great contributions by maximization analysis.

(d, e) Left graphs indicate the averaged total $\Delta F/F$ of all ROIs (b) during all left or right kick events. $\Delta F/F$ was measured from raw data of each event at the ROIs (b) excluding those of the <50 % possibility and the somatosensory area. Then, the $\Delta F/F$ of 11 or 10 trials were all averaged for each hemisphere. The middle or right graphs indicate the averaged total $\Delta F/F$ of the specific cell assembly whose peak of $\Delta F/F$ appeared before or after the initiation of the leg movement (abbreviated as "before group", "after group"). Bold red and blue lines indicate the mean of FI of each 5 frames. The bottom numbers indicate the numbers of the ROIs in the left or right hemisphere within each time period (-3 to -2 / -2 to -1 / -1 to 0 // 0 to 1 / 1 to 2 / 2 to 3 [sec]). The

underlines mean that the number is larger than on the other side. As a result, the lateralized activity was observed, especially at a period from -2 to +2 sec, just before and after the initiation of the motion in left graphs.

These three differential activities are also basically observed in the middle graphs representing the result of the "before group" cell assembly. Surprisingly, however, in the "after group" cell assemblies (right graphs), there was almost no difference in the left-right activities at periods from 0 to +2 sec. In contrast, the "before group" cell assemblies (middle graphs) indicate the different left-right activities before and after the onset of the motion.

In conclusion, our data suggest that motor planning for the left or right hindleg specific movements has been already completed by the lateralized activation of the "before group" cell assembly before the onset of the movement which lasts even after the initiation of the movements. **(f, g)** The "before group" and "after group" cell assemblies of (d, e) were plotted on the schematic diagram of the motor cortical area whose regional compartments are the same as the image of Fig. 8d. The bottom numbers mean the numbers of the ROIs in the left or right hemisphere. The underlines mean that the number is larger than on the other side. As a result, the tendency of the lateralized distribution also appears in the overall qualitative analysis similarly to visual judgment, cross-correlation analysis, and comprehensive quantitative analysis.

In summary, lateralized premotor activities seem to start from M2 on each opposite side of the hemisphere, and the activities propagate to M1 and the somatosensory region. The trends of our results are largely consistent among all the different analyses that were conducted in this paper. The result that the volitional movement originates from M2 is consistent with previous reports and supports them[18,44-46]. The pre- and post-motor activities in M1 have been occasionally pointed out to be non-lateralized[17,47,50], and even ipsilateral[49,50]. In fact, the "after group" cell assemblies of (d, e) show bilateral non-lateralized activity during the period from 0 to +2 sec. However, the "before group" cell assemblies of (d, e) represent differential activity, and the 2D distribution study in Fig. 8f showed that the pre- and post-motor activities in M1 are also lateralized similarly as well as in M2. Therefore, we conclude that M1 activity is lateralized.

The lateralized premotor activity at just before the initiation of the motion (-0.5 to 0 sec) probably represents the start of a direct motor command in the neurons projecting to motor neurons controlling the muscle, and the period includes a point of no return in vetoing the motion (around -0.2 sec)[51]. The direct activity in M1 occurs 50 to 80 ms before muscle movement[52].

Supplementary Movie 1   Examples of imaging the freely moving mouse wearing the HLC and spacer apparatus (Fig. 1c) under various conditions.

Supplementary Movie 2 Ca^{2+} imaging by the HLC over the occipital cortex of an awake CaMK2a-G-CaMP7 mouse (Fig. 1d).

In the movie, (a) shows a movie where the background of the raw imaging movie (10 frame/sec) was subtracted by using ImageJ with a sliding paraboloid (curvature radius is 200 pixels), and was deconvoluted. (b) is one frame of the movie (a). (c) is the magnified movie of the inset shown in (b). (d) is the same as (b). (e) was made by subtracting the FI of each pixel with the average of the FI of the same pixel during the first 10 times.

Supplementary Movie 3   The procedure for counting the number of blinking spots in the view field of Fig. 1d.

In the movie, (a) shows the maximized movie that 8 movies of 1 min were merged by taking the maximum FI for each pixel. (b), (c) show the same image of Supplementary Fig. 3a, b, respectively.

Supplementary Movie 4   x10 Ca^{2+} imaging by the HLC on the 3D cultured G-CaMP6-Hela with histamine administration (Supplementary Fig. 6a, raw fluorescence image is shown in Fig. 4a).

Supplementary Movie 5   x20 Ca^{2+} imaging with a 2-photon microscope over the motor cortex of the anesthetized CaMK2a-G-CaMP7 mouse (Supplementary Fig. 7c).

Supplementary Movie 6   x100 Ca^{2+} imaging by the HLC on the somatosensory cortical area of the anesthetized Thy1-G-CaMP7 mouse (Fig. 4d, raw fluorescence time-lapse image is shown in Supplementary Fig. 6c).

Supplementary Movie 7   Magnified Ca^{2+} imaging by using the HLC with short spacer in the freely moving mouse.

Ca^{2+} imaging of the visual cortex of the CaMK2a-G-CaMP7 mouse was performed by the HLC with the short spacer under the freely moving condition. The 20-fps movie was magnified by the optical zoom (x 2 in comparison with Supplementary Fig 3) and the digital zoom (x 4) is shown (Fig. 5).

Supplementary Movie 8   The Ca^{2+} imaging by the HLC of the frontal cortex in the freely moving CaMK2a-G-CaMP7 mouse (Supplementary Fig. 8b, d).

The left and right movies show a behavior movie of the mouse and the subtracted and averaged Ca^{2+} imaging movie, respectively.

Supplementary Movie 9   x1/10 Ca^{2+} imaging by the HLC on the motor cortical area of the awake CaMK2a-G-CaMP7 mouse (Fig. 8b).

Left/ middle/ right movies show a behavior movie of the mouse, the raw Ca^{2+} imaging movie, and the marked raw Ca^{2+} imaging movie, respectively. In the right movie, the magenta or green dots mean the neuronal activities which start during the before (-4 to 0 sec) or after (0 to +4 sec) the initiation of the motion. Several arrows indicate the dots and its corresponding positions.

Supplementary Movie 10 Ca^{2+} imaging by the single and dual HLC under the freely moving condition.

Real-time Ca^{2+} imaging of the awake CaMK2a-G-CaMP7 mouse by the single HLC of the frontal cortical area (Supplementary Fig. 2d) or by the dual HLC of the frontal and occipital cortical area (Supplementary Fig. 1d) were performed. The movie shows 30-fps captures of the video images displayed on the PC monitor. Judging from the orientation position of the blood vessel, the vibration induced by mouse's movements is not recognized and the view field does not change. Also, even if the two HLCs are used, the movement of the mouse is not impaired.